

Density Profiles of TNG300 Voids across Cosmic Time

OLIVIA CURTIS ^{1,2} BRYANNE McDONOUGH ^{3,2} AND TEREASA G. BRAINERD ²

¹*Department of Astronomy & Astrophysics, The Pennsylvania State University, 251 Pollock Road, University Park, PA 16802, USA*

²*Department of Astronomy & Institute for Astrophysical Research, 725 Commonwealth Ave., Boston University, Boston, MA 02215, USA*

³*Department of Physics, Northeastern University, 360 Huntington Ave, Boston, MA 02115, USA*

ABSTRACT

We present radial density profiles, as traced by luminous galaxies and dark matter particles, for voids in eleven snapshots of the TNG300 simulation. The snapshots span 11.65 Gyr of cosmic time, corresponding to the redshift range $0 \leq z \leq 3$. Using the comoving galaxy fields, voids were identified via a well-tested, watershed transformation-based algorithm. Voids were defined to be underdense regions that are unlikely to have arisen from Poisson noise, resulting in the selection of $\sim 100 - 200$ of the largest underdense regions in each snapshot. At all redshifts, the radial density profiles as traced by both the galaxies and the dark matter resemble inverse top-hat functions. However, details of the functions (particularly the underdensities of the innermost regions and the overdensities of the ridges) evolve considerably more for the dark matter density profiles than for the galaxy density profiles. At all redshifts, a linear relationship between the galaxy and dark matter density profiles exists, and the slope of the relationship is similar to the bias estimates for TNG300 snapshots. Lastly, we identify distinct environments in which voids can exist, defining “void-in-void” and “void-in-cloud” populations (i.e., voids that reside in larger underdense or overdense regions, respectively) and

we investigate ways in which the relative densities of dark matter and galaxies in the interiors and ridges of these structures vary as a function of void environment.

Keywords: Large-scale structure of the Universe (902) – Voids (1779) – Magnetohydrodynamical simulations (1966)

1. INTRODUCTION

Cosmic voids are the largest and emptiest structures in the universe (Tift & Gregory 1976; Gregory & Thompson 1978). They are also excellent cosmological probes due to the fact that, regardless of how a tracer population is defined, the positions and motions of tracers within voids adhere to linear theory at all size scales (e.g., Colberg et al. 2005; Nadathur et al. 2015; Schuster et al. 2023). Because of this, voids have been used for a number of cosmological purposes in both observations and numerical simulations, including estimations of the sum of the neutrino masses (e.g., Villaescusa-Navarro et al. 2013; Schuster et al. 2019; Kreisch et al. 2022), tests of modified theories of gravity (e.g., Li et al. 2012; Clampitt et al. 2013; Zivick et al. 2015; Contarini et al. 2021), constraints on the dark energy equation of state (e.g., Lee & Park 2009; Lavaux & Wandelt 2010; Adermann et al. 2017), deducing values of cosmological parameters (e.g., Park & Lee 2007; Hamaus et al. 2015; Pellicciari et al. 2023; Wang & Pisani 2024), and characterizing the impact of voids on the integrated Sachs-Wolfe effect for the cosmic microwave background (e.g., Kovač et al. 2014; Nadathur et al. 2014; Cai et al. 2017; Owusu et al. 2023).

Voids are interconnected with the flow patterns of the cosmic web (e.g., Bothun et al. 1992; Tully et al. 2019; Vallés-Pérez et al. 2021; Courtois et al. 2023; Schuster et al. 2023). Courtois et al. (2023) used Cosmicflows-3 (Tully et al. 2016) data to study void galaxies in the Calar Alto Void Integral-field Treasury survey (see, e.g., Domínguez-Gómez et al. 2023a; Domínguez-Gómez et al. 2023b) and Tully et al. (2019) used Cosmicflows-3 to study the dynamics of the Local Void (Tully & Fisher 1987), from which they determined that the repulsion from the Local Void greatly contributes to the motion of the Local Group. Both of these studies showed that, in the local universe, the flow in and around voids is primarily dominated by the dynamical tidal influence of nearby filaments and walls, sometimes resulting in a flow field that enters

the void. Therefore, an understanding of the relative densities of dark matter and galaxies in the ridges of voids could help model these flow patterns in the future.

Void density profiles resemble reverse spherical top-hats (Sheth & van de Weygaert 2004; Hamaus et al. 2014; Ricciardelli et al. 2014); that is, they have very underdense centers and ridges that are $\sim 20\%$ more overdense than the average of the survey from which they were obtained. In both simulations and observations, void density profiles have been shown to exhibit this shape regardless of tracer type, and their averaged radial and integrated number density profiles are well modeled by empirical formulae (e.g., Paz et al. 2013; Hamaus et al. 2014; Pollina et al. 2017; Schuster et al. 2023). Understanding the mass density fields of voids is especially important for studies of redshift space distortions around voids (e.g., Hamaus et al. 2015; Correa et al. 2021; Hamaus et al. 2022).

Furthermore, Kaiser (1984) showed that galaxy distributions do not directly mirror the dark matter distribution. That is, on the largest scales, there is a shift between the clustering amplitudes of void tracers and the underlying mass field, where this shift is known as a linear bias when it takes on a constant value. Pollina et al. (2017) found that there is a linear relationship between the dark matter field and the void tracer field from a study of voids in the $z = 0.14$ Magneticum Pathfinder simulation (see, e.g., Dolag et al. 2016 and Hirschmann et al. 2014) and that the slope of the relationship is a good estimate for the clustering bias. Observational confirmation of the relationship found by Pollina et al. (2017) may be possible in the future; this will, however, depend upon precise measurements of weak lensing by voids, allowing direct constraints on their mass distributions to be obtained (see, e.g., Izumi et al. 2013; Barreira et al. 2015; Sánchez et al. 2017; Paillas et al. 2019; Bonici et al. 2023).

Voids also play an important role in modulating cosmic flow patterns (see, e.g., Cautun et al. 2014). In the simplest picture, voids expand and expel material outward into sheets that then drive the material toward filaments and clusters (Zel'dovich 1970; Shandarin & Zeldovich 1989; van Haarlem & van de Weygaert 1993). Several studies have analyzed the evolution voids and how these structures interact with the cosmic web as a whole. For example, Cautun et al. (2014) tracked the mass distributions, velocity fields, and structure sizes within the Millennium simulation (Springel et al. 2005), showing how the mass and volume of the cosmic web evolved from being dominated by tenuous sheets and filaments at early times to being

dominated in volume by voids and in mass by clusters and filaments at later times. They also showed that, compared to halos and filaments in more dense environments at low redshifts, void halos are less massive and void filaments are wider. They attribute this “frozen” structure formation to the fact that void filaments and halos are too far apart and too feeble in mass to merge with neighboring structures, halting the development of medium-scale density fluctuations at low redshifts (Aragon-Calvo & Szalay 2013).

Other authors have tracked the evolution of individual voids across cosmic time (see, e.g., Sutter et al. 2014a; Wojtak et al. 2016). Sutter et al. (2014a) achieved this by tracking the IDs of dark matter particles and identifying which voids share particles from snapshot to snapshot. Using this method, Sutter et al. (2014a) found that typical voids form early, rarely merge, and grow slowly. They also investigated void evolution in terms of the void hierarchy (e.g., Sheth & van de Weygaert 2004), tracking how voids embedded in overdense regions can collapse over time and showing that, compared to voids in denser environments, voids in underdense regions experience more mergers. However, Wojtak et al. (2016) argued that this method of constructing merger trees introduces ambiguity as most particles tend to lie on the boundary of a void and therefore can be exchanged with neighboring voids, leading to spurious reconfigurations of the shapes and positions of voids. Instead, Wojtak et al. (2016) constructed a single void catalog at $z = 0.0$ using a watershed void finding algorithm (Platen et al. 2007) and tracked each watershed basin backward in time to identify the corresponding voids at earlier redshifts. They showed that while the axis ratios of individual voids can change over time by a factor of ~ 0.2 , the overall distribution of void shapes remains the same due to the fact that the more elongated voids tend to become more spherical and vice versa. Wojtak et al. (2016) also showed that the orientations of the void principal axes remain constant over time and that the major and minor axes of nearby voids tend to align with one another at all redshifts.

Lastly, while the depletion of gas from voids has been seen in simulations (van de Weygaert & van Kampen 1993; Padilla et al. 2005) and in observations (see, e.g., Ceccarelli et al. 2006; Patiri et al. 2012; Tully et al. 2019), Vallés-Pérez et al. (2021) showed that at $z = 0$, around 10% of the mass within voids may be accreted from surrounding overdense regions. By analyzing the velocity fields around voids from $z = 100$ to $z = 0$, they show that it is possible for larger surrounding clouds of material to collapse into voids and for sheets and filaments to pass through the outer regions of voids as they collapse towards dense environments. They

also argue that it is possible for events such as galaxy mergers (e.g., [Behroozi et al. 2013](#)) and strong shocks (e.g., [Zhang et al. 2020](#)) to unbind material from massive halos and send it streaming into voids. These results disrupt the idea that voids are pristine environments and are counterintuitive to the picture that voids are simply expanding and expelling material.

In this paper, we present radial profiles of simulated voids that span the redshift range $0.0 \leq z \leq 3.0$. We use the TNG300 Λ Cold Dark Matter simulation to determine the radial dependencies of the galaxy number densities and the dark matter mass densities inside the voids, with the goal of measuring the degree to which galaxies trace the underlying mass fields. TNG300 is the largest simulation box in the IllustrisTNG suite of simulations ([Nelson et al. 2018](#); [Marinacci et al. 2018](#); [Pillepich et al. 2018](#); [Springel et al. 2018](#); [Naiman et al. 2018](#)) and will be discussed further below. We also investigate the effect of void hierarchy on the relative distributions of dark matter and galaxies within the voids. Lastly, we extend the work done by [Pollina et al. \(2017\)](#) to $z = 3.0$ by investigating the relationships between void density profiles, as traced separately by the galaxies and the dark matter, and we compare the slopes of these relationships to clustering bias estimates in TNG300 that were obtained by [Springel et al. \(2018\)](#).

Recently, [Rodríguez-Medrano et al. \(2024\)](#) released TNG300 void catalogs that were obtained with the 3D Spherical Void Finder (3DSVF) developed by [Paz et al. \(2023\)](#). Rather than a 3DSVF, here we elect to use the watershed voidfinding algorithm known as ZOBOV (ZOnes Bordering On Voidness; [Neyrinck 2008](#)). We make this choice because a study by [Douglass et al. \(2023\)](#) showed that, compared to the radial profiles of ZOBOV-identified voids, 3DSVFs produce radial density profiles with [1] flatter interiors and [2] ridges with densities equal to the mean density of the survey in which the voids were found. Since ZOBOV makes no assumptions about void shapes, and also includes the shell-crossing regime in its void profiles, this makes ZOBOV void catalogs well suited for studies of void shapes and dynamics, whereas 3DSVFs are a better option for the study of void galaxies.

The paper is organized as follows. TNG300 and the snapshots that we analyze are discussed in §2. We describe our void-finding algorithm in §3 and the void catalogs in §4. In §5.1, we construct radial number density profiles for the voids using both the dark matter particles and the galaxies as density tracers, and we discuss how the profiles evolve over time. We then divide the voids into two populations based on their

hierarchy in §5.2 and we investigate the dependence of the density profiles on void hierarchy. We summarize and discuss our results in §6.

2. TNG300 SNAPSHOTS

We search for voids in the comoving galaxy fields of eleven snapshots of the highest-resolution TNG300 simulation. TNG300 encompasses a co-moving volume of $205^3 h^{-3} \text{Mpc}^3$. The simulation starts at $z = 127$ with $2,500^3$ dark matter particles of mass $m_{\text{dm}} = 4.0 \times 10^7 h^{-1} M_{\odot}$ and $2,500^3$ hydrodynamical gas cells with initial baryonic mass $m_{\text{b}} = 7.5 \times 10^6 h^{-1} M_{\odot}$ were used. The redshifts, snapshot numbers, lookback times, and softening lengths for each snapshot that we use are summarized in Columns 1-4 of Table 1. The cosmological parameters adopted in the simulation are: $\Omega_{\Lambda,0} = 0.6911$, $\Omega_{m,0} = 0.3089$, $\Omega_{b,0} = 0.0486$, $\sigma_8 = 0.8159$, $n_s = 0.9667$, and $h = 0.6774$ (e.g., [Planck Collaboration et al. 2016](#)). We adopt the subhalo magnitudes from the supplementary catalog of [Nelson et al. \(2018\)](#) to assign luminosities to the galaxies. Compared to the main TNG subhalo catalog, the [Nelson et al. \(2018\)](#) catalog better resembles SDSS photometry because it includes the effects of dust obscuration on the simulated galaxies.

We use the publicly available TNG300 subhalo catalog to identify galaxies. We only search for voids in the comoving galaxy field of each snapshot. We elect to use as a tracer population all subhalos that meet a magnitude and mass cut described below. The sparsity and bias of tracers influence void detection such that voids that are identified in a sparse and heavily biased tracer population will yield fewer voids, which are larger on average, compared to those produced using a less biased tracer population ([Sutter et al. 2014b](#); [Nadathur & Hotchkiss 2015](#); [Pollina et al. 2016](#); [Pollina et al. 2017](#)). The relatively small box-size of TNG300 is the limiting factor for our study as the most biased tracers in the simulation are too rare to properly trace the large-scale structure. Indeed, at $z = 0.0$, there are only ~ 240 groups more massive than $10^{14} h^{-1} M_{\odot}$ (i.e., objects the TNG team considers to be galaxy clusters). The small volume of TNG300 also limits the total number of voids that we can identify. An advantage of this simulation is that it generates subhalos which precisely reproduce global galaxy clustering ([Springel et al. 2018](#)) and population statistics ([Nelson et al. 2018](#)), in part due to its precise mass resolution elements. We thus expect to find fewer voids that are smaller compared to studies that have identified voids in other hydrodynamical simulations (see, e.g., [Schuster et al. 2023](#)), but we will be able to better predict the distribution of galaxies within and around voids.

A robust description of baryonic processes in hydrodynamic simulations requires resolution elements that are capable of modeling the small-scale radiative and feedback processes that affect galaxy evolution (Nelson et al. 2018). Void catalogs have historically been made under the assumption that galaxy voids can be reliably compared to void catalogs built on halos in dark matter simulations (Panchal et al. 2020), but modern simulations have allowed for resolved subhalo void catalogs to be constructed from boxes $\gtrsim 100\text{Mpc}$, enabling the effects that baryonic processes and tracer selection have on void statistics to be measured directly. (see, e.g., Paillas et al. 2017; Habouzit et al. 2020; Panchal et al. 2020; Rodríguez Medrano et al. 2022; Schuster et al. 2023; Curtis et al. 2024; Rodríguez-Medrano et al. 2024). To construct our tracer population, we first exclude all luminous objects that are flagged as non-cosmological in origin (i.e., those with `SubhaloFlag` set to 0). These are objects identified by the `Subfind` algorithm (Springel et al. 2001) that may not have formed due to large-scale structure formation or collapse and are instead fragments of material that have formed within an existing halo through baryonic processes and are usually low mass, baryon dominated, and located near the centers of their host halos.¹ With the exception of the $z = 3.0$ snapshot, we also exclude galaxies with absolute r -band luminosities $M_r \geq -14.5$ and stellar masses $\leq 10^8 h^{-1} M_\odot$. Here, stellar mass is defined as the total mass of the stellar particles that are bound to a subhalo. We chose to use a cut on stellar mass rather than a cut on total mass as the former is an observable quantity that can be obtained by modeling galaxy spectral energy distributions. Our chosen cut ensures that each galaxy contains a reasonable minimum number of stellar particles (~ 15 for $z \leq 2.0$) and that there are enough galaxies present in the snapshot for the void finding algorithm to converge on a solution. At $z = 3.0$, relatively few galaxies exist in TNG300; therefore, in order to have a sufficient number of galaxies such that we can identify voids at $z = 3.0$, we adopt a minimum stellar mass of $10^{7.75} h^{-1} M_\odot$, corresponding to ~ 10 stellar particles, for this snapshot.

Void shapes and sizes are known to depend on tracer density (see Sutter et al. 2014b). As our tracer number densities decrease from $\sim 0.040 h^3 \text{Mpc}^{-3}$ at $z = 0.0$ to $\sim 0.037 h^3 \text{Mpc}^{-3}$ at $z = 0.7$, $\sim 0.027 h^3 \text{Mpc}^{-3}$ at $z = 1.5$, and $0.014 h^3 \text{Mpc}^{-3}$ at $z = 3.0$, we expect to find larger voids at earlier redshifts. As Sutter et al.

¹ For more details, see <https://www.tng-project.org/data/docs/background/#subhaloflag>

(2014b) note, at $z = 0$ when dark matter and halos are used as tracers, sparser sampling primarily produces voids with slightly denser ridges. These results were more pronounced for voids larger than $30h^{-1}$ Mpc and for tracer densities (n_t) sparser than $n_t \lesssim 10^{-3}$. Compared to our catalogs at redshifts < 1 , we might expect our catalogs at redshifts > 1 to have denser ridges. However, given the fact that we have relatively high tracer densities that produce galaxy voids with radii $\sim 15 - 20h^{-1}$ Mpc, we do not expect these mass cuts to have a significant effect on void radial profiles. Moreover, studies that identify voids out to high redshifts (see, e.g., Sutter et al. 2012; Nadathur 2016; Mao et al. 2017) must overcome a similar falloff in tracer density with redshift due to Malmquist bias. We thus expect our catalogs, when viewed from $z = 3.0$ to $z = 0.0$, to better reflect such attempts at void identification.

3. VOIDFINDING ALGORITHM

We use the ZOnes Bordering On Voidness (ZOBOV) algorithm (Neyrinck 2008) to identify TNG300 voids. ZOBOV is based on the Watershed Void Finder (Platen et al. 2007) and finds voids using a Voronoi Tessellation Field Estimator (Schaap 2007). The algorithm makes no assumptions about the shape or symmetry of voids, which allows for amorphously shaped voids to be identified. Throughout, we implement ZOBOV using the publicly available code REVOLVER² (Nadathur et al. 2019), and we summarize the algorithm below.

First, the code determines the local density around each galaxy using a Voronoi Tessellation Field Estimation (see, e.g., Schaap 2007). The Voronoi tessellation draws cells around each galaxy so that each cell contains one galaxy and the regions of space that are closest to this galaxy. The density estimate around galaxy i is then $1/V(i)$ where $V(i)$ is the volume of Voronoi cell around galaxy i .

Next, the code locates the density minima (i.e., the Voronoi cells with the smallest density estimate) and defines these cells to be zone cores. Then, neighboring cells with density estimates that are higher than the zone core are added to the zone. This process is repeated with the new zone boundaries such that any cell with a density estimate larger than a neighboring zone cell is also considered part of that zone. This step ends when no cell with a larger density estimate than the cells that comprise the boundary of the zone is

² <https://github.com/seshnadathur/Revolver>

Table 1. TNG300 Snapshots and Void Statistics

Redshift	Snap. No.	t_{lookback} (Gyr)	$r_{\text{softening}}$ ($h^{-1}\text{kpc}$)	N_{gal}	n_t ($h^3\text{Mpc}^{-3}$)	N_{voids}	$N_{\text{voids,significant}}$	Volume	N_{VIC}	N_{VIV}
0.0	99	0.00	1.0	342635	0.040	1065	174	39.5%	88	86
0.1	91	1.34	1.1	338602	0.039	1056	178	37.1%	90	88
0.2	84	2.51	1.2	334219	0.039	1075	166	35.4%	92	74
0.3	78	3.53	1.3	329227	0.038	1047	159	33.7%	88	71
0.4	72	4.41	1.4	325406	0.038	1059	158	33.0%	91	67
0.5	67	5.19	1.5	322657	0.037	1091	145	30.4%	85	60
0.7	59	6.49	1.7	315329	0.037	1093	165	32.9%	96	69
1.0	50	7.94	2.0	295677	0.034	1059	173	40.0%	106	67
1.5	40	9.52	2.0	229435	0.027	935	123	31.6%	63	60
2.0	33	10.51	2.0	170014	0.020	750	96	28.0%	52	44
3.0	25	11.65	2.0	118841	0.014	607	70	29.6%	36	34

found. The result of this step is that there is always a positive density gradient going outwards from a zone core to the boundary of the zone.

Zones can then be combined to form voids, but there has historically been no consensus on how to control such merging and different methods are known to affect void parameters (Nadathur & Hotchkiss 2015). The process of merging involves adding to a zone all neighboring zones with a minimum Voronoi cell density estimate greater than the minimum density estimate of the starting zone. Like the previous step in the algorithm, this step is repeated for zones on the boundary of the newly constructed void until it can no longer annex additional zones. In order to obtain a usable catalog of non-overlapping voids, it is necessary to introduce some parameters to halt the merging process (Nadathur & Hotchkiss 2014). Otherwise, a final ZOBOV void is a collection of all zones of increasing density away from the void center, and excludes the highest-density ridge that separates it from other voids. This produces a hierarchy of voids and sub-voids, ranging from many smaller voids to one void that encompasses the entire simulation volume. Methods to halt merging include using the $P(r)$ statistic (described in more detail below), which measures the probability that any given underdense region is a relic of Poisson noise (Neyrinck 2008), as a means to gauge when the growth of a void should be halted. Another strategy is to grow voids until the density of the most underdense Voronoi cell along the ridge separating it from a shallower potential is greater than 0.2 times the mean tracer density of the population (Sutter et al. 2015). However, as Nadathur & Hotchkiss (2015) point out, preventing merging provides a definition of voids that rely solely on the topology of the density field, simplifying the model. As such, REVOLVER performs no merging and instead defines a void as any zone that has a volume greater than the median value of all zones (see, e.g., Nadathur & Hotchkiss 2014).

As a final pruning step, we compute a cumulative probability that a REVOLVER void arose due to Poisson fluctuations. Since the distribution of underdensities in a Poissonian density contrast field is unknown, Neyrinck (2008) calculated the cumulative probability using Monte Carlo sampling of Poissonian data. Neyrinck (2008) defined the cumulative probability function, $P(r)$, of the ratio, r , between the density of the lowest-density Voronoi cell on the ridge connecting a void to a deeper neighboring void and the minimum density of the void. This ratio is always greater than 1 (i.e., the ridge of a void region will always be more

dense than the center of the void). For the deepest void in a sample, the lowest-density Voronoi cell on the ridge connecting it to its deepest neighbor is used to calculate r . In three dimensions, $P(r)$ is given by

$$P(r) = \exp[-5.12(r - 1) - 0.8(r - 1)^{(2.8)}] . \quad (1)$$

[Neyrinck \(2008\)](#) interprets this as the fraction of voids in a Poisson distribution with density contrast ratios greater than r . That is, $P(r)$ is the likelihood that an underdense region with ratio r could arise due to Poisson noise, with smaller values of $P(r)$ indicating a higher likelihood that the void is spurious. This distribution resembles a half-normal distribution that is centered on $r = 1$ with a peak of $P(r) = 1$ (see Figure 2 of [Neyrinck 2008](#)). Thus, $P(r)$ has “standard deviations” analogous to standard deviations of Gaussian distributions. For example, at 1σ significance, 31.7% of voids have a density contrast ratio greater than 1.22, and 68.3% of voids have a density contrast ratio less than 1.22. For our voids, we adopt a significance level of 2σ . That is, we reject all voids with $P(r) < 4.55 \times 10^{-2}$. This significance level was chosen to be consistent with other studies that have used this technique (see, e.g., [Mao et al. 2017](#)). A lower threshold would admit more voids with low-density cores, while a higher threshold would further restrict our catalogs to only contain voids that show the clearest contrast between core density and linking density. The latter of these thresholds would have reduced our void counts to $\sim 20 - 50\%$ of their current values. A 2σ cut also ensures that most ($\sim 95\%$) voids in the sample have central density contrasts $\lesssim -0.8$ and thus strikes a balance between void counts and removing artifacts of Poisson noise.

4. VOID CATALOGS

The results of applying ZOBOV to the galaxy fields of each snapshot are summarized in Table 1. Here, columns 1-4 show the redshift, snapshot number, look back times, and softening lengths for the 11 snapshots of interest, and columns 5-11 show the number of galaxies that meet the resolution criteria from §2, the resulting tracer number density (n_t), the total number of voids found by ZOBOV, the number of voids that meet our void significance threshold, the percent of the volume of the simulation occupied by significant voids, the number of “voids-in-clouds”, and the number of “voids-in-voids” (see §5.2). On average, significant voids occupy 33.7% of the simulation volume.

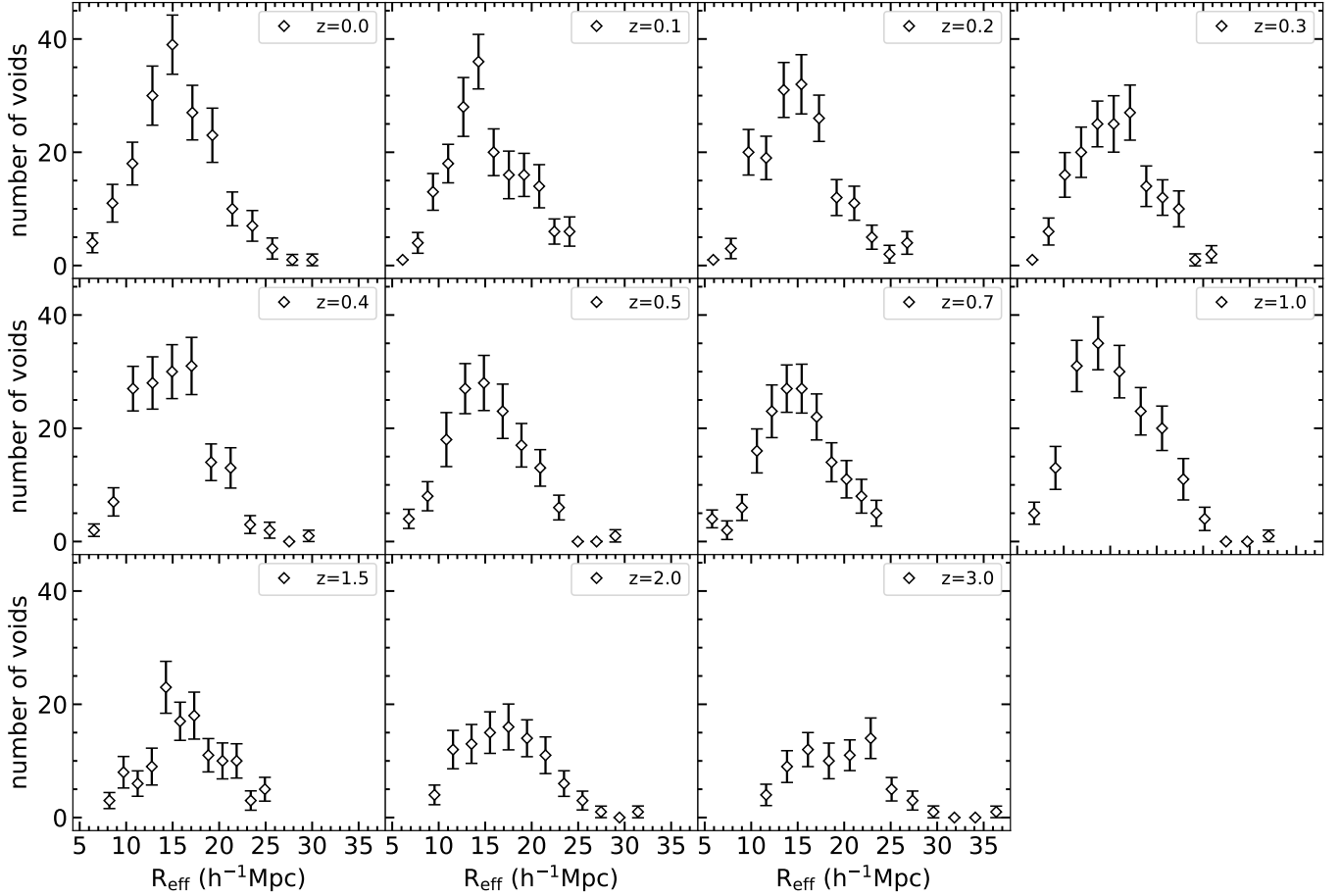


Figure 1. Distributions of void effective radii, r_v , for each snapshot. Error bars are calculated from 10,000 bootstrap resamplings of the data.

The average number of significant voids per snapshot is 147 ± 11 . For the most part, the total number of significant voids increases over time. At the earliest redshifts, there is an increase from 70 significant voids at $z = 3.0$ to 123 at $z = 1.5$, then at lower redshifts $\sim 145 - 175$ significant voids are identified in each snapshot. The smaller number of voids identified at the earliest redshifts is likely attributable to the fact that fewer galaxies exist in these snapshots, leading to the identification of fewer voids at earlier redshifts. Since the galaxy field is sparser at high redshifts than it is at low redshifts, this also results in the high redshift voids being systematically larger on average than the low redshift voids (see below).

We begin our analysis by computing the effective radii, R_{eff} , for the significant voids. Here, R_{eff} is defined to be the radius of a sphere whose volume is identical to that of the (amorphously shaped) ZOBOV void. Since the voids were identified in co-moving coordinates, the values of R_{eff} are co-moving radii. Figure 1

shows a mosaic of the distributions of void effective radii from all eleven snapshots. Each panel shows the distribution of all significant voids in a given snapshot in bins of widths $2h^{-1}$ Mpc. From Figure 1, the void effective radii are roughly normally distributed. Over time, the maxima of the distributions increase to just under 20 between $z = 3.0$ and $z = 1.5$, where they remain throughout the rest of the snapshots. The maxima of the distributions for redshifts $z \leq 1.0$ all occur at $R_{\text{eff}} \sim 15h^{-1}\text{Mpc}$.

Figure 2 shows the median values of R_{eff} as function of redshift and lookback time. The median effective void radius decreases from $\sim 20h^{-1}\text{Mpc}$ at $z = 3.0$ to $\sim 15h^{-1}\text{Mpc}$ at $z = 1.0$, where it remains for the rest of the snapshots. As discussed above, the fact that, on average, voids at earlier redshifts are systematically larger than they are at lower redshifts is due to the fact that there are fewer galaxies in the earliest snapshots. In reality, individual voids should increase in size over time as they expand and merge with surrounding voids (Sheth & van de Weygaert 2004). However, since we are constrained by the resolution of the TNG300, we are limited by the number of galaxies we can use to identify the voids.

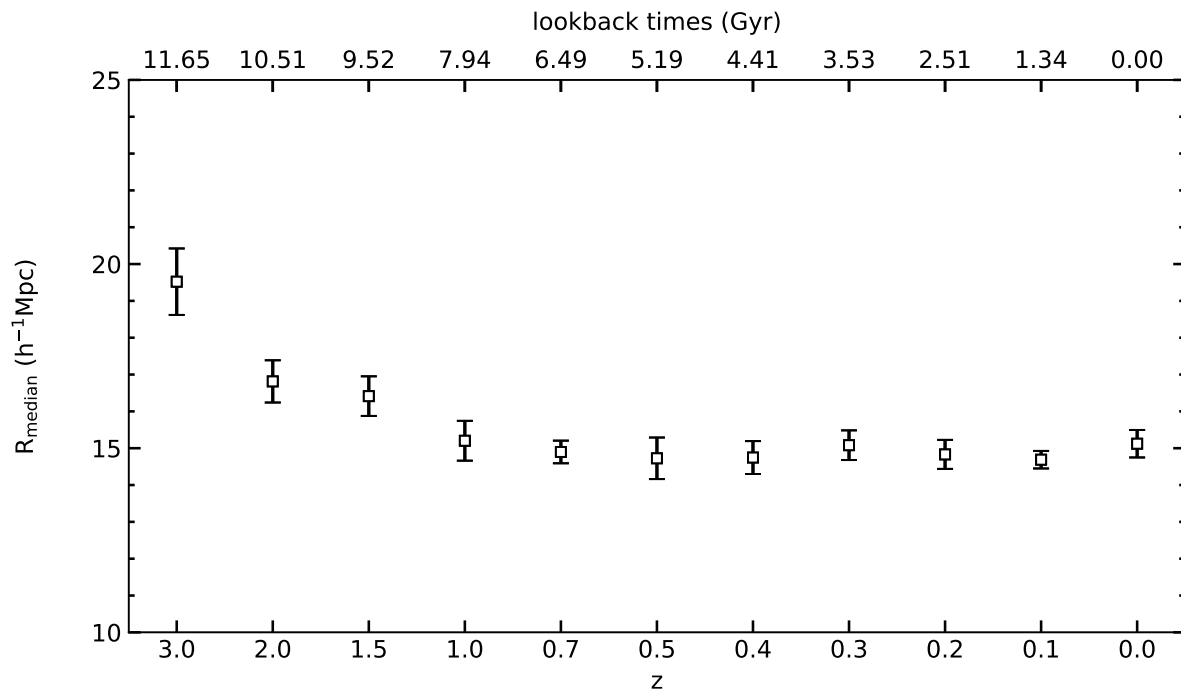


Figure 2. Median R_{eff} of TNG300 voids as a function of redshift and lookback time. Error bars are calculated from 10,000 bootstrap resamplings of the data.

5. EVOLUTION OF VOID RADIAL AND INTEGRATED PROFILES

5.1. Radial Density Profiles

As must be done in observational studies, we identified TNG300 voids using the spatial distributions of the galaxies. In order to investigate the degree to which light traces mass within the voids, however, we use both the galaxies and the dark matter particles to trace the radial density profiles. Below we will refer to the density profiles as traced by the galaxies as “luminous matter profiles” and the density profiles as traced by the dark matter particles as “dark matter profiles”. We define a void center as the center of the largest sphere within a void that is completely devoid of galaxies (see, e.g., [Nadathur et al. 2015](#); [Nadathur 2016](#); [Nadathur et al. 2019](#)). This was chosen over a volume-weighted barycenter following [Nadathur et al. \(2015\)](#) who argued that, compared to a barycentric definition, this minimum density definition gives a better estimate for the true location of the matter underdensity within a void. We define the radial density profiles as the number density contrast of, respectively, the galaxies and the dark material particles that are contained within radial bins, centered on each void center. That is, the radial dependence of the density contrast (i.e., the void-tracer cross-correlation function) is defined as

$$\delta = \frac{n(r)}{\bar{n}} - 1. \quad (2)$$

Figure 3 shows the density contrast profiles (top) as well as the integrated number density contrast profiles (bottom) for all voids in the $z = 0.0$ snapshot (dashed lines). The left panels use dark matter particles as the tracer population while the right panels use galaxies. Here, the error bars represent the standard error of the mean data while the shaded regions show the middle 68% range of the data. For the integrated density profiles, we classify voids as “void-in-cloud” if they are embedded within a larger overdense region and as “void-in-void” if they are embedded within a larger underdense region (see §5.2). The range of individual density profiles closely matches the variety of density profiles seen in similar studies (see, e.g., [Paz et al. 2013](#); [Dávila-Kurbán et al. 2023](#)). Most deviations arise within void ridges where the density contrasts can vary between $\sim -0.6 - 1.5$. Beyond the ridge, the density profiles tend toward the average of the surrounding environment. For most voids, this is a density contrast of 0, but the profiles for “voids-in-clouds” can tend

toward values > 0 at large distances due to the fact that these voids are embedded in an overdense region by definition. Despite our small sample size and the range of our individual void profiles, the mean void profiles are relatively localized and thus serve as a good metric for studying the distribution of material in and around voids.

Figure 4 shows average void radial density profiles for each of the eleven snapshots. Green diamonds show the results obtained using galaxy counts and purple circles show the results obtained from the dark matter particles. The error bars show the standard errors of the mean profiles and the shaded regions show the middle 68% ranges of the data. As expected, these density profiles resemble the reverse spherical top-hat distribution at all redshifts. While the interiors of voids remain nearly devoid of galaxies ($\delta < -0.9$) across all redshifts, the void centers are more underdense in dark matter particles at later times than they are at earlier times. Despite having $\lesssim 123$ voids at redshifts $z \leq 1.5$, the dark matter density profiles maintain a relatively narrow range of density contrasts. Over time, the dark matter exits void cores and is deposited into void ridges, increasing the diversity of the individual dark matter profiles such that the ranges of the dark matter profiles become more comparable to those of the galaxy profiles at later times. The ranges of the galaxy profiles also broaden with time, especially at radii $\gtrsim 1r_v$, but the changes are not as noticeable as they are for the dark matter profiles. The mean galaxy profiles do not appear to evolve noticeably with time, although there are slight fluctuations from redshift to redshift that we will discuss below, but the mean dark matter profiles do evolve to have more underdense cores and more overdense ridges at later times. Below, we discuss the evolution of these mean profiles, focusing on how the maximum and minimum density contrasts of each profile evolve over time.

Figure 5 presents summary statistics for the average radial density profiles in Figure 4. Panels a) and c) of Figure 5 show the maximum and minimum density contrasts of the profiles, while panels b) and d) show the ratios of $\delta_{\min,DM}/\delta_{\min,galaxies}$ between the corresponding points in panels a) and c). Figure 5a) demonstrates that the dark matter density contrast of the ridges of voids evolved over time. As traced by the dark matter, the ridges have an average maximum density contrast of $\delta_{\max} = 0.055 \pm 0.01$ at $z = 3$. This increases to 0.178 ± 0.03 at $z = 0.7$ and 0.240 ± 0.041 at $z = 0.2$ before decreasing to 0.138 ± 0.033 at $z = 0.0$. The galaxy profiles show a similar trend, increasing from 0.161 ± 0.035 at $z = 3.0$ to 0.286 ± 0.044 at $z = 0.2$ before

decreasing to 0.176 ± 0.039 at $z = 0.0$. Because of this, the ratios of $\delta_{\min, \text{DM}}/\delta_{\min, \text{galaxies}}$ in Figure 5b) slowly increase by a factor of ~ 2 from $z = 3.0$ to $z = 0.0$.

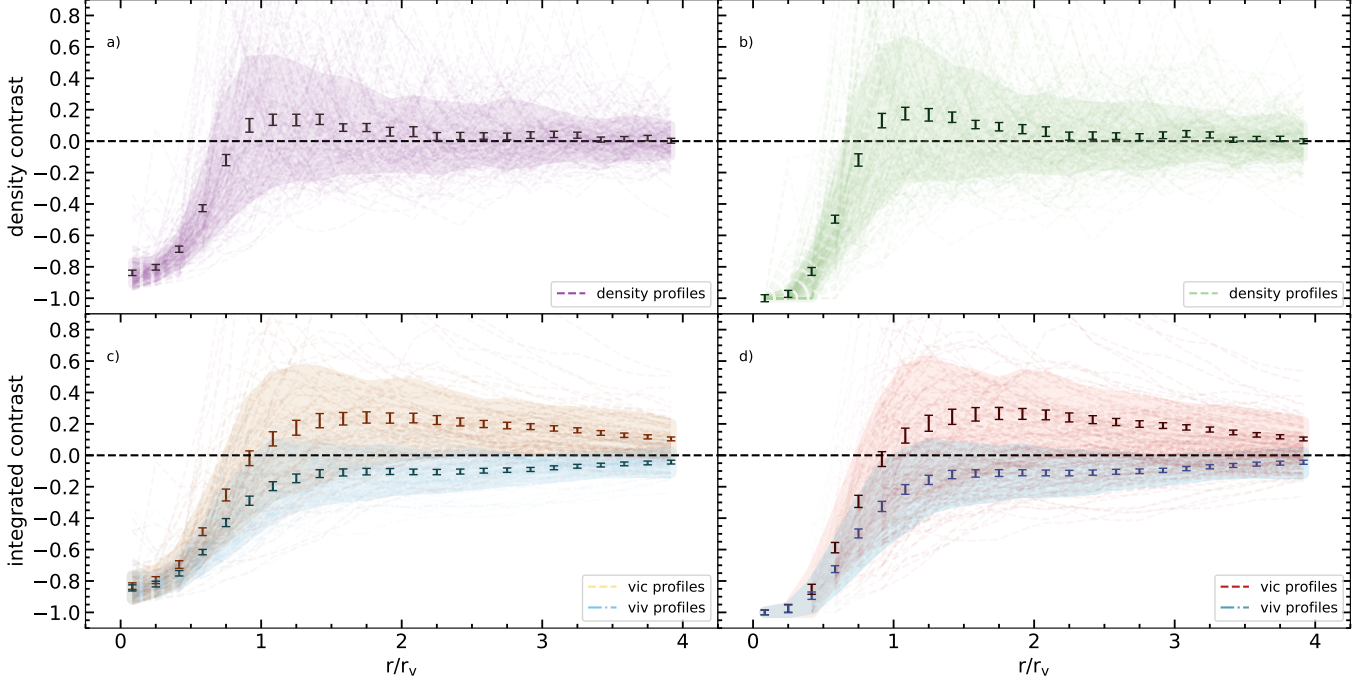


Figure 3. Density contrast profiles (top) and integrated density profiles (bottom) for all significant voids in the $z = 0.0$ snapshot. Panel a): dark matter density contrast profiles (dashed purple lines). Panel c): integrated dark matter density profiles for the “void-in-cloud” (dashed orange lines, see text) and “void-in-void” (dot-dashed blue lines) populations. Panel b): galaxy density contrast profiles (green). Panel d) integrated galaxy density profiles for the “void-in-cloud” (red) and “void-in-void” (blue) populations. The error bars represent the standard error of the mean data and the shaded regions show the middle 68% range of the data.

An exception to this is an apparent decrease of δ_{\max} between redshifts $z = 0.2 - 0.0$. An evolution of density profiles could indicate a shift of the maximum density to slightly larger radii. To investigate this, we plot R_{\max} (i.e., the center of the radial shell at which $\delta = \delta_{\max}$) in Figure 6a). Here, green diamonds and purple circles show R_{\max} for the galaxy profiles and dark matter profiles, respectively, and the error bars show the radial bin widths of $\sim 0.08R_{\text{eff}}$. R_{\max} remains within 1 radial bin of $1.25 \pm 0.08R_{\text{eff}}$ for all profiles over time. With the exception of the $z = 0.0$ snapshot, R_{\max} aligns for both the galaxy and dark matter profiles. While we do see an increase in R_{\max} for galaxies at $z = 0.0$, we see no indication that the densest

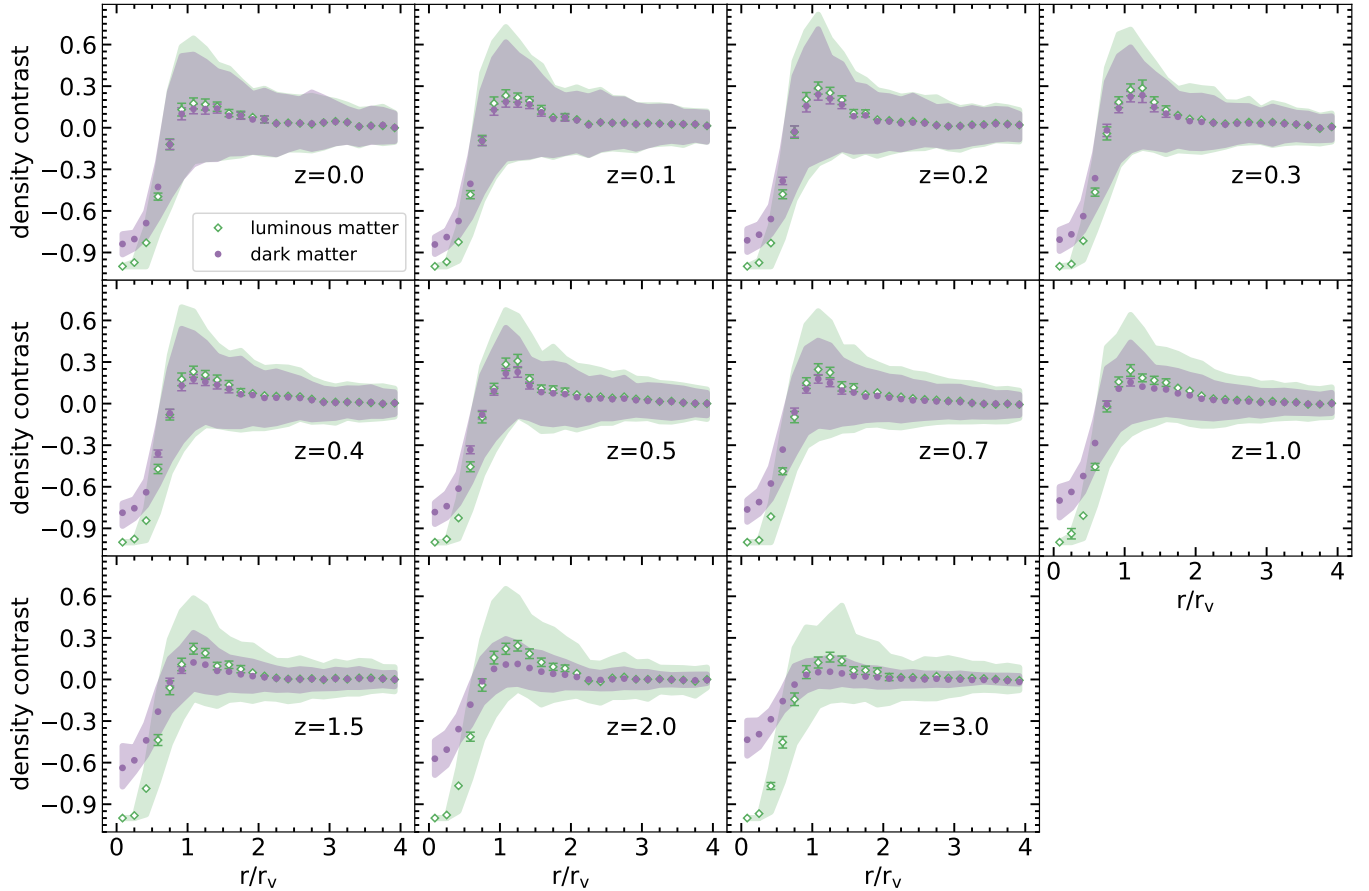


Figure 4. Average radial number density profiles of TNG300 voids across time. Green diamonds: galaxies are used as density tracers. Purple circles: dark matter particles are used as density tracers. Error bars: standard error of the mean density profile. Shaded regions: middle 68% range of the data.

shells surrounding voids evolve to larger radii at later times. However, as we will see in §5.2, the integrated density profiles do suggest that R_{\max} increases between $z = 0.3 - 0.0$.

The average minimum density contrasts in Figure 5c) occur in the central regions of the voids. Because of this, δ_{\min} represents the density of material in the innermost regions of the voids. Across all redshifts, galaxies are especially rare within the centers of voids; i.e., the luminous matter profiles approach density contrasts of -1 at small distances from the void centers. This could be an artifact of our void sampling as the cut that we imposed with equation 1 preferentially selects voids with underdense cores relative to their ridges. However, despite having nearly empty interiors, Figure 3b) shows that even voids with rarefied cores can sharply increase in density as early as $0.3r_v$. The interiors of voids on the other hand are underdense

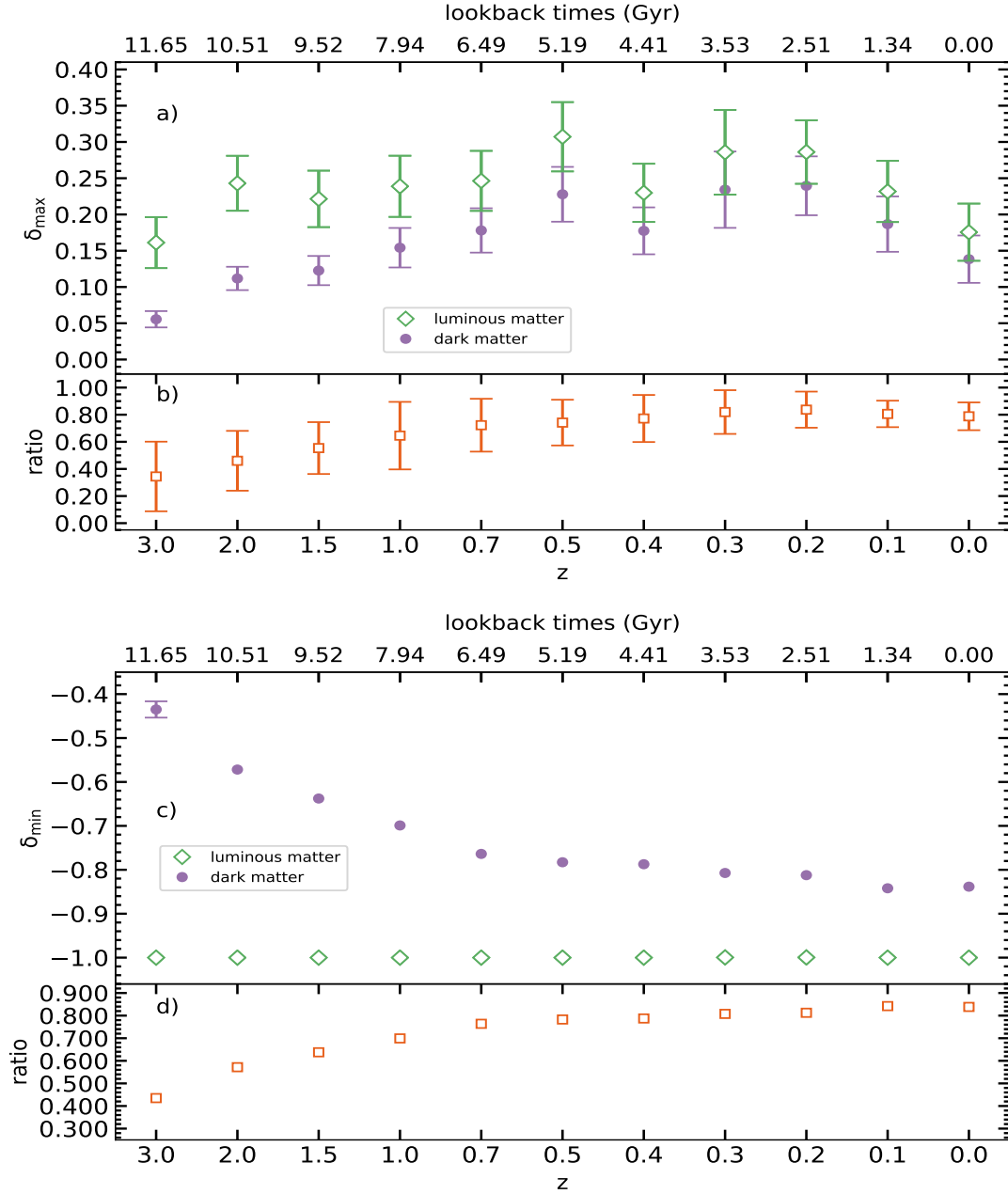


Figure 5. Panels a) and c) show the average maximum and minimum density contrast of all void profiles over time when galaxies (diamonds) and dark matter particles (circles) are used as tracers of the density contrast. Panels b) and d) show the ratios between the corresponding points in panels a) and c).

in dark matter, they are not completely empty of dark matter, and they become increasingly bereft of dark matter over time. From Figure 5c), most of the changes in the interior dark matter density occur between $z = 3.0$ and $z = 0.7$. That is, at $z = 3.0$, the average minimum dark matter density contrast is -0.42 , while it

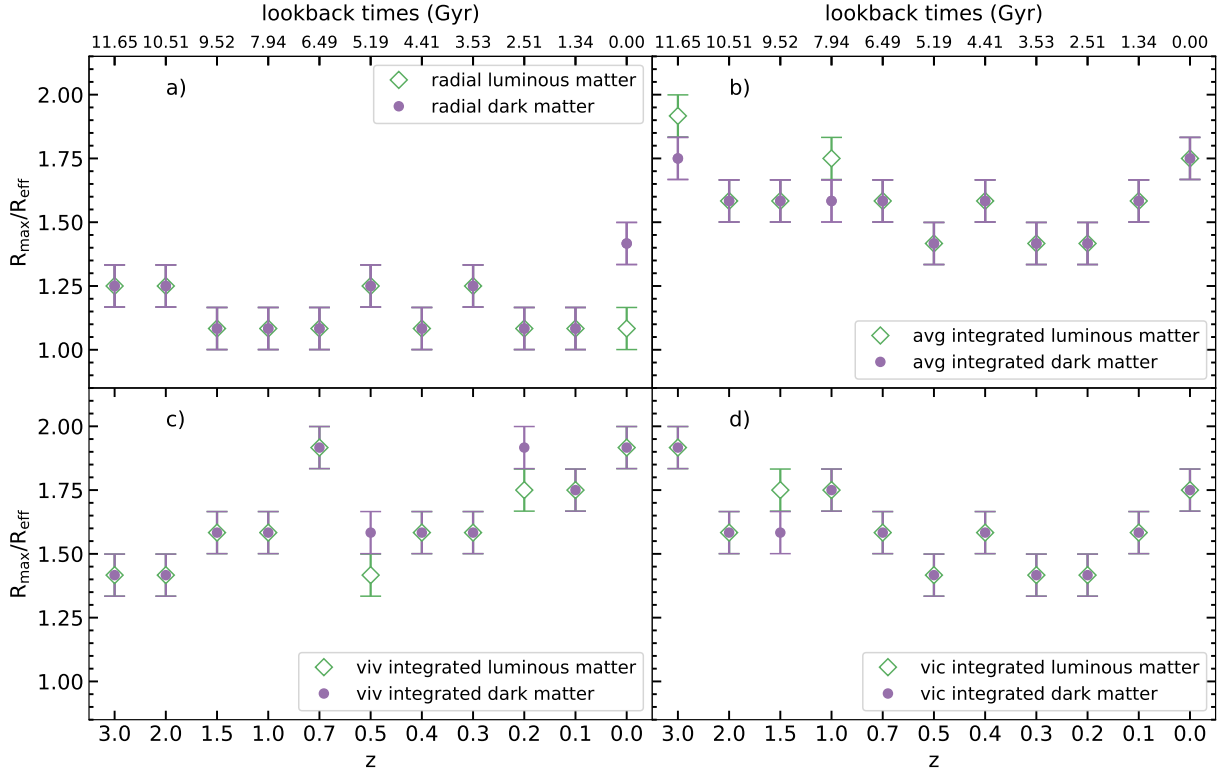


Figure 6. Panel a): the centers of the radial shells at which $\delta = \delta_{\max}$ for the radial density profiles when galaxies (diamonds) and dark matter particles (circles) are used as tracers. Vertical bars show the bin widths used when creating Figure 4. Panels b)-d): the radii of the maximum-density spheres of the integrated density profiles over time (see text). Vertical bars show the bin widths used in constructing Figure 8. Panel b): all integrated density profiles. Panel c): “voids-in-voids.” Panel d): “voids-in-clouds.”

is -0.76 at $z = 0.7$, and -0.82 at $z = 0.0$. Thus, the ratios of $\delta_{\min, \text{DM}}/\delta_{\min, \text{galaxies}}$ in Figure 5d) increase by a factor of ~ 2 from $z = 3.0$ to $z = 0.0$.

Pollina et al. (2017) showed that, within voids, luminous tracers of the void density contrast are linearly correlated with the matter density contrast. Pollina et al. (2017) found this to be true when galaxies, clusters, or active galactic nuclei were used as tracers. Further, they showed that the slope of this relationship, b_{slope} , is a good estimate for the linear bias factor that arises from a consistent shift between the clustering amplitude of the density tracers and the underlying mass field (see, e.g., Peebles 1980; Kaiser 1984; Mo & White 1996; Tinker et al. 2010). That is, they found that the equation

$$\delta_{\text{tracer}} = b_{\text{slope}}\delta_{\text{DM}} + c_{\text{offset}} \quad (3)$$

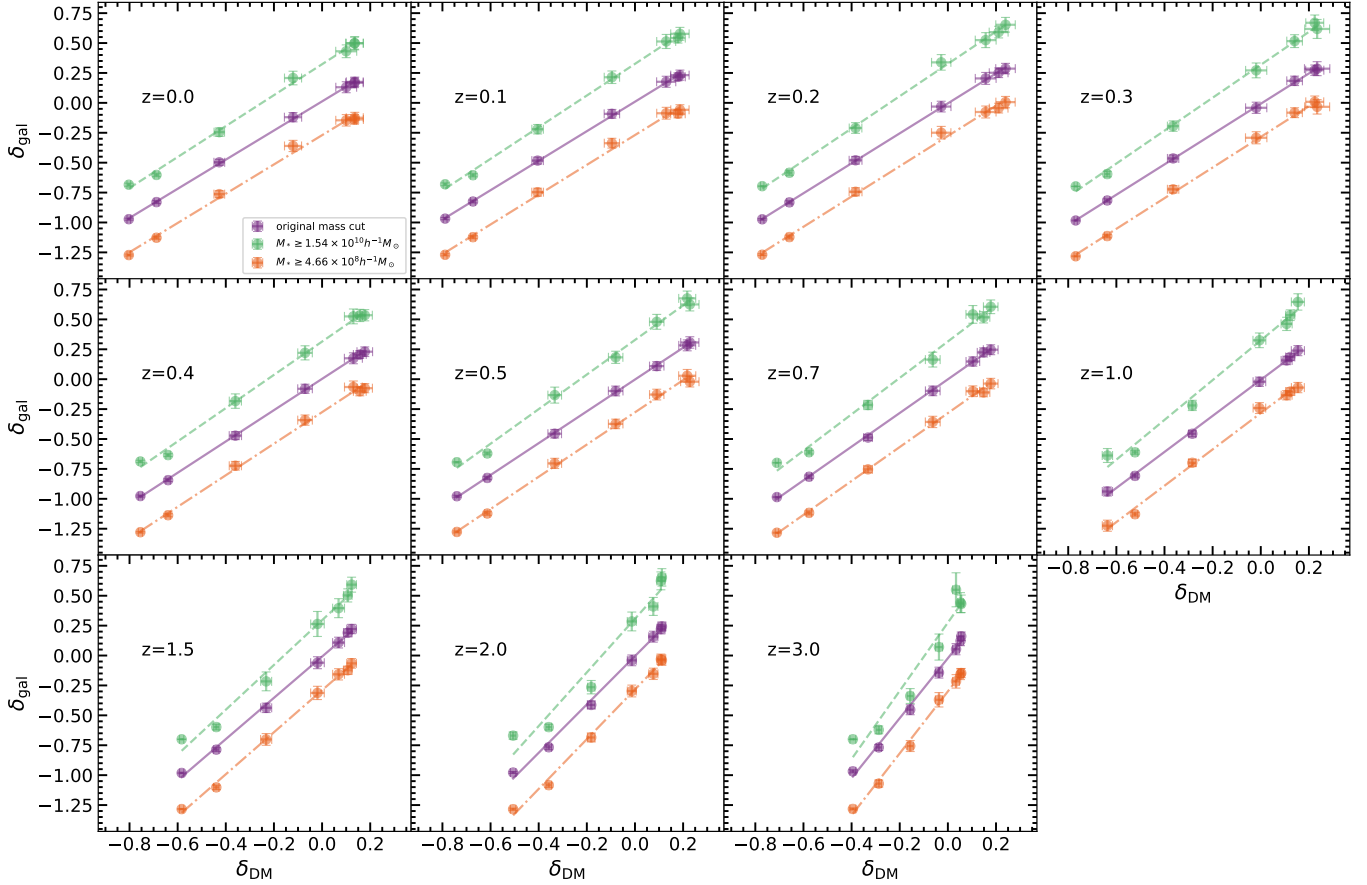


Figure 7. Void galaxy density contrasts vs. dark matter density contrasts in each snapshot. Points: average galaxy and dark matter radial density contrasts in spherical shells with radii between $0.1 - 1.2R_{\text{eff}}$. Minimum density contrasts correspond to void centers; maximum density contrasts correspond to ridges (see Figure 4). Lines correspond to best-fit lines. Purple: original mass cut (see § 3). Green: galaxies with stellar masses $\geq 1.54 \times 10^{10} h^{-1} M_{\odot}$. Orange: galaxies with stellar masses $\geq 4.66 \times 10^8 h^{-1} M_{\odot}$. For clarity, the green (orange) points and the green (orange) lines have been linearly shifted up (down) by 0.3.

holds for all voids in the **Magneticum Pathfinder** simulation at $z = 0.14$. Here, δ_{tracer} is the void tracer density contrast, δ_{DM} is the dark matter density contrast, b_{slope} is the slope of the linear relationship, and c_{offset} is the intercept of the relationship (which is usually within a few percent of zero).

To determine whether our **TNG300** voids show a similar linear relationship, we plot δ_{gal} vs δ_{DM} using the data reported above in Figure 7 (plotted in purple). In addition, to facilitate a comparison with the results of [Springel et al. \(2018\)](#) below, we recalculate our void-galaxy cross-correlation functions using as tracer populations only the galaxies with stellar masses $\geq 4.66 \times 10^8 h^{-1} M_{\odot}$ and $1.54 \times 10^{10} h^{-1} M_{\odot}$, and

Table 2. Best-fitting linear relationships between for equation 3.

Redshift	original mass cut				$M_* \geq 4.66 \times 10^8 h^{-1} M_\odot$				$M_* \geq 1.54 \times 10^{10} h^{-1} M_\odot$			
	N_{gal}	b_{slope}	c_{offset}	R^2	N_{gal}	b_{slope}	c_{offset}	R^2	N_{gal}	b_{slope}	c_{offset}	R^2
0.0	342635	1.22 ± 0.01	0.01 ± 0.01	0.999	226171	1.22 ± 0.04	0.03 ± 0.02	0.996	41450	1.29 ± 0.03	0.02 ± 0.01	0.996
0.1	338602	1.23 ± 0.01	0.01 ± 0.01	0.999	222690	1.25 ± 0.04	0.03 ± 0.02	0.996	39878	1.32 ± 0.03	0.03 ± 0.01	0.997
0.2	334219	1.25 ± 0.01	0.00 ± 0.01	0.999	218070	1.27 ± 0.03	0.02 ± 0.01	0.996	38327	1.35 ± 0.03	0.03 ± 0.01	0.998
0.3	329227	1.27 ± 0.01	-0.01 ± 0.01	0.999	212056	1.28 ± 0.03	0.02 ± 0.01	0.998	36536	1.38 ± 0.03	0.02 ± 0.01	0.997
0.4	325406	1.31 ± 0.01	0.00 ± 0.01	0.999	205199	1.32 ± 0.03	0.02 ± 0.01	0.997	34609	1.39 ± 0.04	0.01 ± 0.02	0.996
0.5	322657	1.33 ± 0.01	0.00 ± 0.01	0.999	197583	1.35 ± 0.03	0.02 ± 0.01	0.997	32458	1.45 ± 0.05	0.03 ± 0.02	0.995
0.7	315329	1.41 ± 0.02	0.00 ± 0.01	0.999	183228	1.42 ± 0.03	0.02 ± 0.01	0.998	28148	1.52 ± 0.06	0.02 ± 0.02	0.991
1.0	295677	1.51 ± 0.02	-0.01 ± 0.01	0.999	163949	1.52 ± 0.05	0.02 ± 0.02	0.995	22058	1.66 ± 0.09	2.46 ± 0.03	0.986
1.5	229435	1.72 ± 0.04	-0.01 ± 0.01	0.998	121871	1.76 ± 0.04	0.01 ± 0.01	0.998	14210	1.87 ± 0.10	-0.01 ± 0.03	0.985
2.0	170014	2.02 ± 0.06	0.00 ± 0.02	0.996	84488	2.08 ± 0.07	0.02 ± 0.02	0.995	8920	2.24 ± 0.21	0.01 ± 0.05	0.957
3.0	118841	2.51 ± 0.09	-0.02 ± 0.02	0.994	35505	2.59 ± 0.08	0.00 ± 0.02	0.996	2952	2.85 ± 0.32	-0.02 ± 0.06	0.941

we plot these data in Figure 7 in orange and green, respectively. For clarity, the green (orange) points and line have been linearly shifted up (down) by 0.3. Figure 7 shows δ_{gal} vs. δ_{DM} for the average void profile from each snapshot, and the dashed lines are best-fit linear relationships. That is, each point in Figure 7 shows the galaxy and dark matter radial density contrasts in concentric spherical shells with radii between $0.1 - 1.2R_{\text{eff}}$, such that the minimum density contrasts correspond to void centers and the maximum density contrasts correspond to ridges (see Figure 4). A linear trend between δ_{gal} and δ_{DM} exists at all redshifts for all 3 tracer populations, and the slope of the relationship generally increases between sequential snapshots. Below, we show that this increasing slope indicates a larger clustering bias between galaxies and dark matter at high redshifts. Table 2 shows the number of tracers, b_{slope} , and c_{offset} for each snapshot, along with the R^2 statistics for the fits. Here, the left columns correspond to the results when galaxies in the original mass cut are used as tracers (i.e., galaxies with stellar masses $\geq 10^8 h^{-1} M_{\odot}$ at $z < 3.0$ and $\geq 10^{7.75} h^{-1} M_{\odot}$ at $z = 3.0$), while the center (right) columns show the results when galaxies $\geq 4.66 \times 10^8 h^{-1} M_{\odot}$ ($\geq 1.54 \times 10^{10} h^{-1} M_{\odot}$) are used as tracers.

Springel et al. (2018) calculated the clustering bias within TNG300 using halos and galaxies as density tracers. These were selected based on several resolution cuts to the virial mass, stellar mass, instantaneous star formation rates, and specific star formation rates. The resolution cuts imposed by Springel et al. (2018) correspond to galaxy (or halo) densities that cover the ranges of ongoing and upcoming surveys. They perform a series of mass cuts such that the number density of tracers within each snapshot corresponds to $0.03 h^3 \text{Mpc}^{-3}$ or $0.003 h^3 \text{Mpc}^{-3}$. At $z = 0.0$, this corresponds to a stellar mass cut of $4.66 \times 10^8 h^{-1} M_{\odot}$ and $3 \times 10^{-2} h^3 \text{Mpc}^3$, respectively. Springel et al. (2018) then define a scale-dependent bias model of the form

$$b(k) = b_0 + \beta \left(\ln \frac{k}{k_0} \right)^2, \quad (4)$$

where b_0 is the large-scale linear bias, β is the strength of the scale dependence, k is a wave number, and $k_0 = 0.02 h \text{Mpc}^{-1}$ is the wave number where $db(k)/dk = 0$. Since we fix our tracer number densities to be equal to theirs at $z = 0.0$, we can directly compare our b_{slope} values with their reported values of $b(k)$. For galaxies with stellar masses $\geq 4.66 \times 10^8 h^{-1} M_{\odot}$ ($\geq 1.54 \times 10^{10} h^{-1} M_{\odot}$), they fit $b_0 = 1.17$ ($b_0 = 1.36$) and $\beta = -0.0007$ ($\beta = 0.0016$). If the wave number is $0.067 h \text{Mpc}^{-1}$, which corresponds to the typical size scales

of our voids, the value of $b(k)$ is 1.17 (1.38), while we report a corresponding value of $b_{\text{slope}} = 1.22 \pm 0.4$ ($b_{\text{slope}} = 1.29 \pm 0.03$).

When we use galaxies with stellar masses $\geq 4.66 \times 10^8 h^{-1} M_{\odot}$ as a density tracer, we obtain slopes that are very close to the bias estimates reported by [Springel et al. \(2018\)](#). That is, using the same selection criteria as ours and at typical length scales for our voids, [Springel et al. \(2018\)](#) report a scale-dependent bias parameter of 1.17 at $z = 0.0$, while we report a value of $b_{\text{slope}} = 1.22 \pm 0.04$. When we use as a tracer population galaxies with stellar masses $\geq 1.54 \times 10^{10} h^{-1} M_{\odot}$, our b_{slope} estimate deviates from the results of [Springel et al. \(2018\)](#) ($b(k) = 1.38$ vs. $b_{\text{slope}} = 1.29 \pm 0.03$).

Had we employed either of these stellar masses during our void identification, then the sparser tracer populations would have increased the average sizes of our reported voids. As [Springel et al. \(2018\)](#) note, even at higher redshifts where the bias is more prominent, the bias of the galaxies in TNG300 becomes independent on distance scales larger than $\sim 1 - 10 h^{-1} \text{Mpc}$. As our voids are already larger than this ($\sim 15 - 20 h^{-1} \text{Mpc}$), we do not expect the bias to change at higher size scales. However, [Pollina et al. \(2017\)](#) report that b_{slope} , as measured from galaxy voids in the Magneticum Pathfinder simulation that were identified with the ZOBOV algorithm, decreases with increasing void size up to void sizes $\gtrsim 60 h^{-1} \text{Mpc}$ where it becomes independent of void size. Unfortunately, the limited size of the TNG300 simulation makes such an analysis impossible even if we had used a sparser tracer population during void identification, so we do not attempt to do so here.

The relationship between b_{slope} and the bias parameter is expected to occur in the linear regime of density fluctuations. Thus, our results are in agreement with [Pollina et al. \(2017\)](#) and [Pollina et al. \(2019\)](#), demonstrating that the assumption of linear bias between the galaxies and dark matter within voids holds for voids defined from the density field. Here, we have shown that this assumption continues to hold out to $z = 3.0$.

5.2. Integrated Profiles

In this section, we define two void populations: “voids-in-voids” and “voids-in-clouds” using the same selection of galaxies that we used in §3. These structures correspond to underdensities in galaxy distributions

that are embedded, respectively, within larger underdensities or overdensities (see, e.g., [Sheth & van de Weygaert 2004](#); [Paz et al. 2013](#)).

Using galaxies and dark matter particles as density tracers, we calculate integrated number density contrast profiles, $\Delta(r)$, separately for “voids-in-voids,” “voids-in-clouds,” and the entire void population. That is, $\Delta(r)$ includes the total number of tracer objects in concentric spheres of radius, r , centered on the void centers. “Voids-in-clouds” form from the collapse of larger overdensities, while “voids-in-voids” arise from the expansion and merging of underdense regions, meaning the surrounding velocity field is a useful tool to distinguish void type. In the linear regime, the velocity profiles of voids are proportional to $-\Delta(r)$ ([Peebles 1980](#); [Peebles 1993](#)), making the integrated density profile a well-established proxy for both void hierarchy (see, e.g., [Sheth & van de Weygaert 2004](#); [Ceccarelli et al. 2013](#); [Paz et al. 2013](#); [Dávila-Kurbán et al. 2023](#); [Curtis et al. 2024](#)) and void velocity profiles (see, e.g., [Sheth & van de Weygaert 2004](#); [Paz et al. 2013](#); [Hamaus et al. 2014](#); [Schuster et al. 2023](#)). Using the criteria from [Sheth & van de Weygaert \(2004\)](#) and [Ceccarelli et al. \(2013\)](#), we define “voids-in-voids” to be those with integrated galaxy density contrasts < 0 at $r = 3R_{\text{eff}}$ and “voids-in-clouds” to be those with integrated galaxy density contrasts > 0 at $r = 3R_{\text{eff}}$. Columns 10 and 11 of [Table 1](#) list the total number of “voids-in-clouds” and “voids-in-voids,” respectively. From [Table 1](#), there are more “voids-in-clouds” than “voids-in-voids,” with an average ratio of 4 : 3 for each snapshot.

[Figure 8](#) shows the average integrated profiles for each void population. Points show the results when galaxies are used as density tracers, and solid lines show the results when dark matter particles are used as density tracers. Red points and orange lines show profiles for “voids-in-clouds,” green points and green lines show profiles for the entire void population, and blue points and blue lines show profiles for the “voids-in-voids.”

Each distribution resembles a reverse spherical top-hat distribution, and similarities and differences exist between the void populations. First, in all cases, the interiors of each void population are nearly empty of galaxies and they are underdense, but not completely devoid of, dark matter. Secondly, at a given redshift (with the exception of $z = 1$), all three luminous profiles converge to nearly identical interior integrated density contrasts, and the same holds true for the dark matter profiles. However, the integrated density

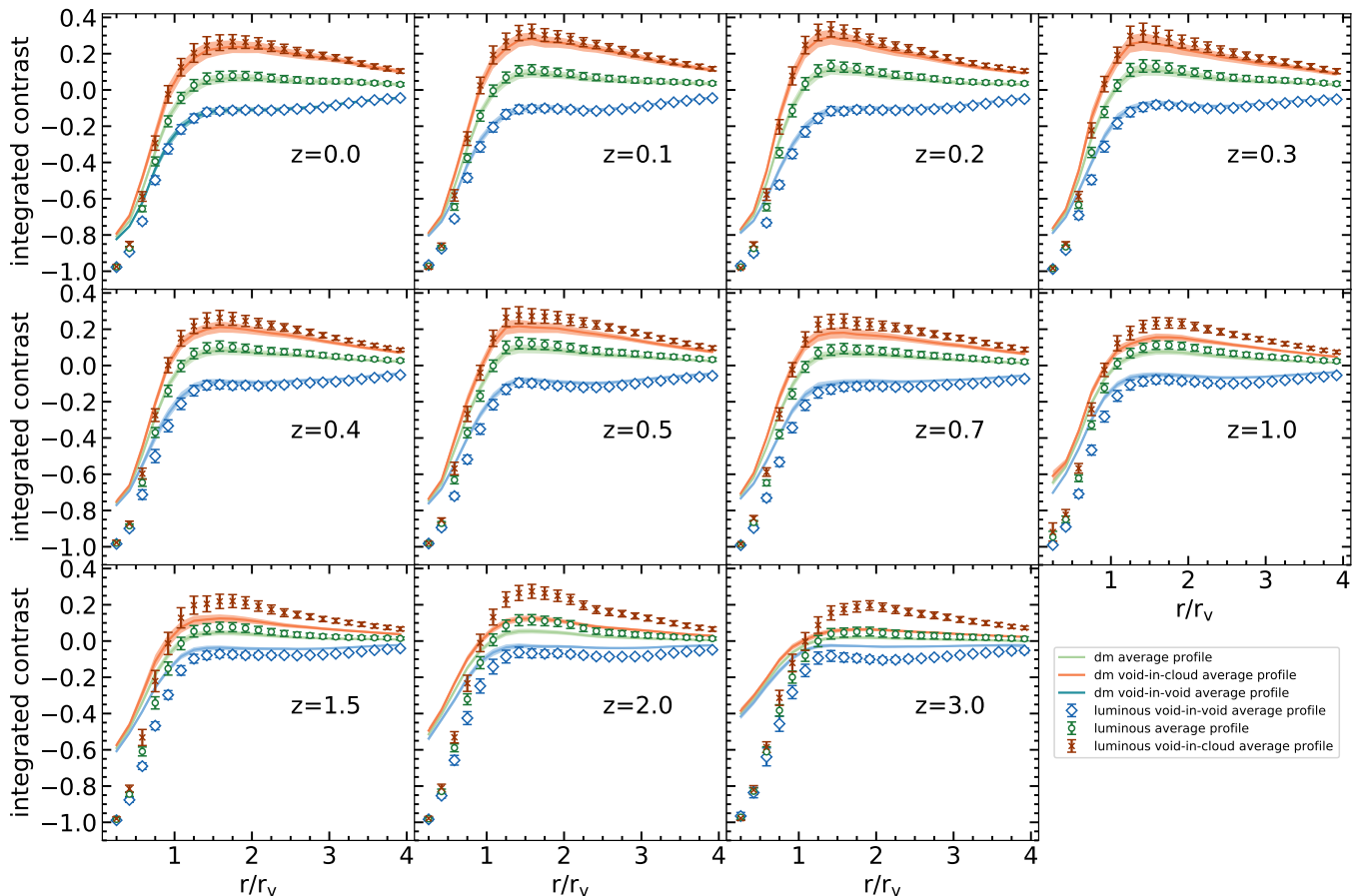


Figure 8. Integrated density profiles for “voids-in-voids,” “voids-in-clouds,” and the entire void population when galaxies (points) and dark matter particles (lines) are used as density tracers. Error bars and shaded regions show the standard error of the mean dark matter and galaxy profiles, respectively. Red points and orange lines: “voids-in-clouds.” Green points and green lines: the entire void population. Blue points and blue lines: “voids-in-voids.”

contrasts of the three void populations (for a given tracer) begin to deviate noticeably from each other for $r \gtrsim 0.5R_{\text{eff}}$. That is, the “void-in-cloud” profiles rapidly increase in luminous and dark matter integrated density, and they peak at integrated density contrasts ~ 0.30 . In contrast, the “void-in-void” profiles increase only gradually beyond $r \sim 0.5R_{\text{eff}}$ and reach density contrasts of ~ -0.2 . Thirdly, there is a higher integrated density of galaxies than dark matter at the void ridges in the “void-in-cloud” and total void populations, whereas dark matter has a larger integrated density contrast than galaxies in the ridges of “voids-in-voids.”

Lastly, regarding redshift evolution, the integrated dark matter density profiles tend to align more closely with their corresponding integrated galaxy density profiles over time. That is, while the centers of voids

remain nearly devoid of galaxies at all redshifts, the dark matter profiles steadily decrease from ~ -0.4 at $z = 3.0$ to ~ -0.7 at $z = 0.7$ and ~ -0.8 at $z = 0.0$. Similarly, the differences between the integrated dark matter and galaxy profiles along void ridges tend to decrease over time. At $z = 3.0$, the ridges of “voids-in-clouds” have a mean integrated galaxy density of ~ 0.2 and a mean integrated dark matter density of ~ 0.06 , while at $z = 0.2$, the mean integrated galaxy density of these voids is ~ 0.34 and the integrated dark matter density is ~ 0.29 .

We examine the time evolution of these profiles in more detail in Figure 9, Figure 10, and Figure 11. Each Figure is formatted in the same way as Figure 5. In discussing these figures, we will refer to the sphere at which the maximum number density contrast occurs as the “maximum-density sphere” and the sphere at which the minimum number density contrast occurs as the “minimum-density sphere.”

Figure 9a) shows the integrated density contrasts of maximum-density spheres for the entire void sample. These maximum-density spheres extend to just beyond R_{eff} . From Figure 9a), the maximum-density spheres contain somewhat less dark matter at early redshifts than at $z = 0.0$. That is, Δ_{max} for the dark matter is 0.019 ± 0.007 at $z = 3.0$, 0.046 ± 0.014 at $z = 1.5$, 0.112 ± 0.028 at $z = 0.2$, and 0.066 ± 0.023 at $z = 0.0$. The maximum-density spheres for the galaxies fluctuate around 0.052 ± 0.024 at $z = 3.0$ to 0.0132 ± 0.030 at $z = 0.3$ and 0.079 ± 0.025 at $z = 0.0$. The ratios of $\Delta_{\text{min,DM}}/\Delta_{\text{min,galaxies}}$ shown in Figure 9b) thus increase over time. Here, the ratios asymptotically approach a value of 0.84 ± 0.23 at low redshifts.

Figure 6b) shows the radii of the maximum-density spheres (R_{max}) used to calculate Δ_{max} for the integrated profiles described above. Here, diamonds (circles) show R_{max} when galaxies (dark matter particles) are used as tracers and bars show the bin widths used in Figure 8. With the exception of the $z = 3.0$ and $z = 1.0$ snapshots, the values of R_{max} for the dark matter profiles are equal to those calculated for the galaxy profiles. At redshifts $z \leq 2.0$, R_{max} remains within one radial bin of $1.58 \pm 0.08R_{\text{eff}}$. For both the dark matter and the galaxy profiles at $z = 0.2$, R_{max} steadily increases from $1.42 \pm 0.08R_{\text{eff}}$ to $1.58 \pm 0.08R_{\text{eff}}$ at $z = 0.1$ and $1.75 \pm 0.08R_{\text{eff}}$ at $z = 0.0$. This correlates with the decrease in Δ_{max} that we report for these redshifts in Figure 9, indicating a mean shift of R_{max} to slightly larger radii at lower redshifts.

Figure 9c) shows the density contrasts in minimum-density spheres. These minimum-density spheres all have radii $r \leq 0.25R_{\text{eff}}$. They are almost completely devoid of galaxies across all redshifts and consistently

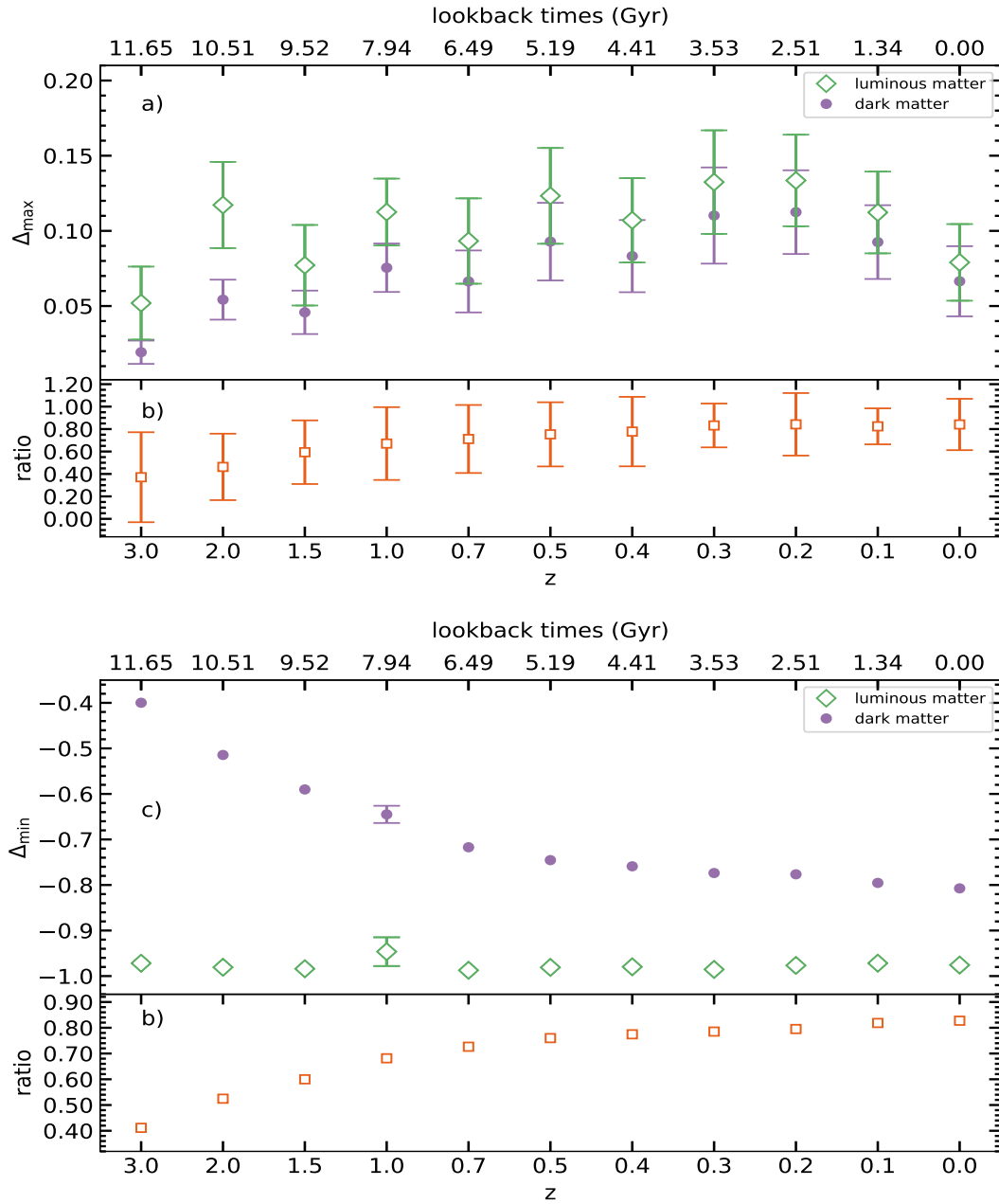


Figure 9. Same as Figure 5 except for all integrated void profiles.

have galaxy number density contrasts of ~ -0.98 . This is not the case for the minimum-density spheres for the dark matter, which have density contrasts that decrease significantly over time. For instance, the integrated dark matter profile decreases from $\Delta_{\min} = -0.400 \pm 0.012$ at $z = 3.0$, to $\Delta_{\min} = -0.807 \pm 0.007$ at $z = 0.0$. Consequently, the ratios of $\Delta_{\min, \text{DM}} / \Delta_{\min, \text{galaxies}}$ in Figure 9d) increase over time.

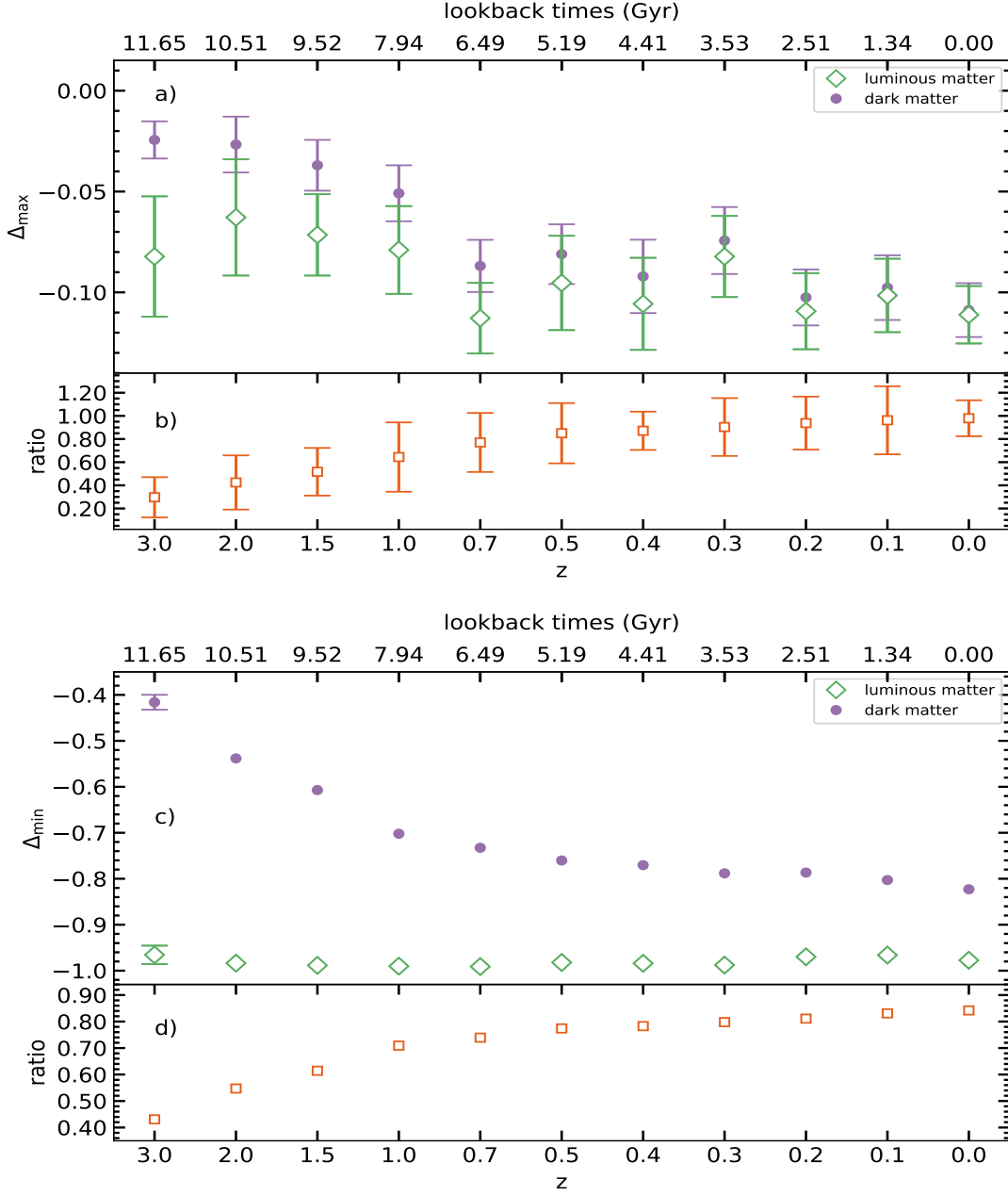


Figure 10. Same as Figure 5 except for all integrated “void-in-void” profiles.

Figure 10a) shows the average integrated density contrasts within maximum-density spheres of “voids-in-voids.” Here, we impose a maximum radius of $r \sim 2.3R_{\text{eff}}$ because some of the integrated “void-in-void” profiles have ridges that are underdense in both galaxies and dark matter compared to the average of the simulation. This means their integrated profiles continue to increase towards unity at radii much larger than the void radii. From Figure 10a), the value of Δ_{\max} for the dark matter shows a trend that is different to

the trend in Figure 9a). Here, Δ_{\max} decreases over time from a maximum of -0.024 ± 0.009 at $z = 3.0$ to -0.109 ± 0.013 at $z = 0.0$. The densities of the maximum-density spheres for galaxies again fluctuate from redshift to redshift. These spheres have density contrasts that start at -0.082 ± 0.030 at $z = 3.0$ but change to -0.063 ± 0.029 at $z = 2.0$, -0.113 ± 0.017 at $z = 0.7$, -0.082 ± 0.020 at $z = 0.3$, and -0.111 ± 0.014 at $z = 0.0$. The ratios of $\Delta_{\min,DM}/\Delta_{\min,galaxies}$ in Figure 10b) thus increase over time. Figure 6c) shows R_{\max} for these spheres. With some exceptions, R_{\max} for both profiles generally increase from $1.42 \pm 0.08R_{\text{eff}}$ at $z = 3.0$ to a maximum of $1.92 \pm 0.08R_{\text{eff}}$ at $z = 0.0$. Exceptions include the jump in R_{\max} at $z = 0.7$ and the $z = 0.5$ and $z = 0.2$ snapshots where R_{\max} for the dark matter and galaxy profiles are not aligned. Thus, even “voids-in-voids” exhibit overdense ridges surrounding them, but as we will see for the ridges of “voids-in-clouds,” “void-in-void” ridges are far less pronounced and peak at higher values of R_{\max} at redshifts $z \leq 0.3$.

Figure 10c) shows Δ_{\min} for “voids-in-voids.” Like the entire void population, these minimum-density spheres all have radii $r \leq 0.25R_{\text{eff}}$. From Figure 10c), Δ_{\min} values for galaxies remain constant at ~ -0.98 across time. However, the value of Δ_{\min} for dark matter decreases from -0.416 ± 0.016 at $z = 3.0$ to a value of -0.823 ± 0.008 at $z = 0.0$. Similar to what is seen in the entire void population, the ratios of $\Delta_{\min,DM}/\Delta_{\min,galaxies}$ in Figure 10d) rise from $z = 3.0$ to $z = 0.0$.

Figure 11a) shows the average integrated number density contrasts within the maximum-density spheres of “voids-in-clouds.” Here, the maximum-density spheres have radii $r \leq 1.5R_{\text{eff}}$. The trends in Δ_{\max} for these voids closely resemble those of the entire void population in Figure 9a). Here, Δ_{\max} for the dark matter increases from an integrated density contrast of 0.064 ± 0.008 at $z = 3.0$ to 0.281 ± 0.035 at $z = 0.1$ and 0.2391 ± 0.035 at $z = 0.0$. The average Δ_{\max} for galaxies shows a similar trend, changing from 0.196 ± 0.026 at $z = 3.0$ to 0.334 ± 0.042 at $z = 0.2$ to 0.267 ± 0.039 at $z = 0.0$. Thus, the ratios of $\Delta_{\max,DM}/\Delta_{\max,galaxies}$ in Figure 11d) increase over time. Figure 6d) shows the values of R_{\max} for these maximum-density spheres. With the exception of $z = 1.5$, R_{\max} for the dark matter and density profiles align with each other. While the values of R_{\max} fluctuate from snapshot to snapshot, the decrease in Δ_{\max} between redshifts $0.2 - 0.0$ again correlates with an increase in R_{\max} , again suggesting that the ridges of the voids tend towards larger radii at later times.

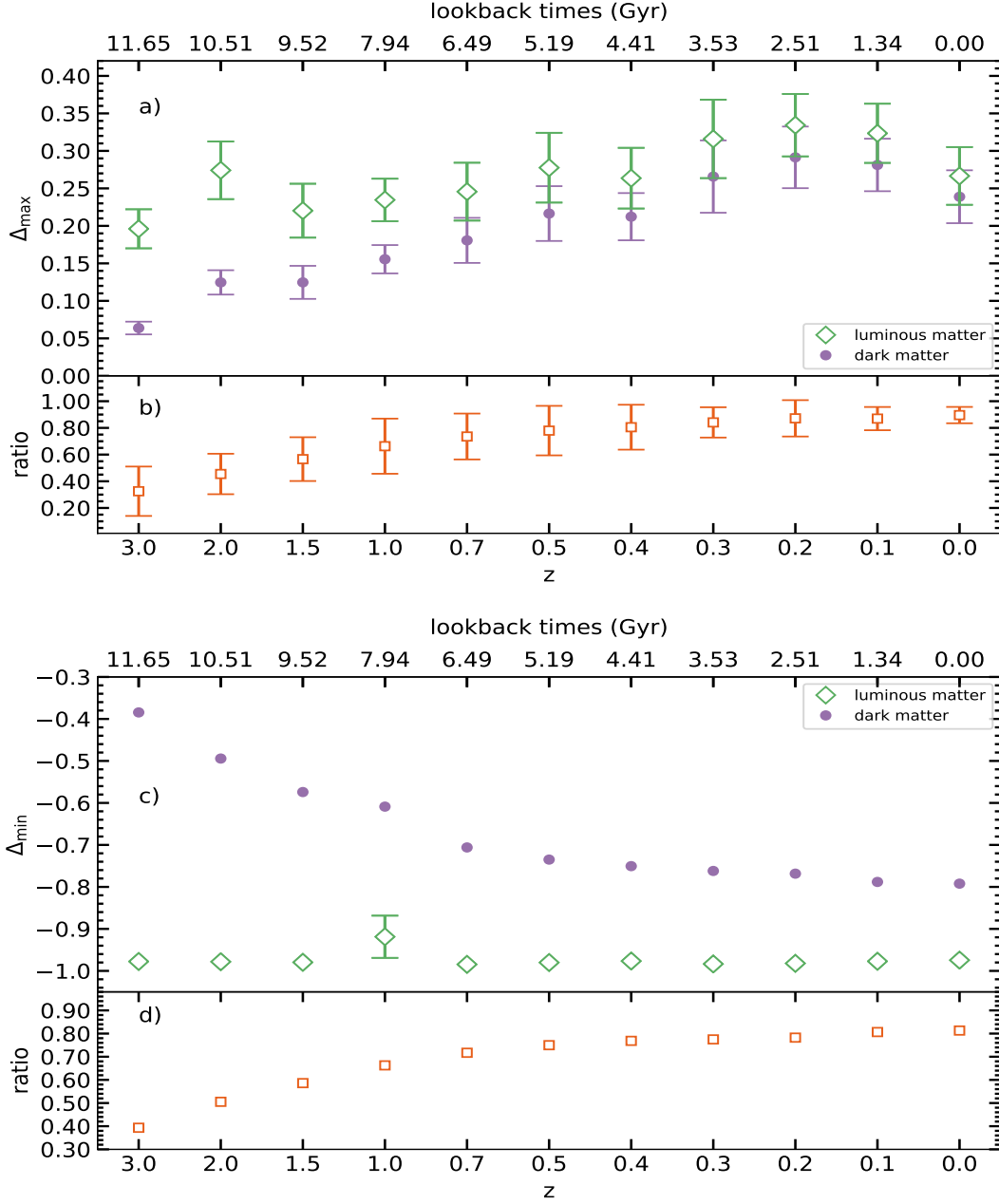


Figure 11. Same as Figure 5 except for all integrated “void-in-cloud” profiles.

Finally, Figure 11c) shows the evolution of Δ_{\min} for “voids-in-clouds.” As with the entire void population, these minimum-density spheres all have radii $r \leq 0.25R_{\text{eff}}$. “Voids-in-clouds” show the same trends as those seen in Figure 9c) and Figure 10c). That is, Δ_{\min} for the dark matter decreases from -0.384 ± 0.015 at $z = 3.0$ to a plateau of -0.792 ± 0.011 at lower redshifts and the Δ_{\min} value for the galaxies remains at -0.98 over time. Thus, the ratios of $\Delta_{\min, \text{DM}}/\Delta_{\min, \text{galaxies}}$ in Figure 11d) increase from $z = 3.0$ to $z = 0.0$.

6. SUMMARY & DISCUSSION

We used the ZOBOV algorithm to identify voids in the galaxy fields of eleven snapshots of the TNG300 simulation. The snapshots span the redshift range $0 \leq z \leq 3$, corresponding to 11.65 Gyr of cosmic time. We find that the galaxy distribution does not directly trace the dark matter distribution within the voids at any redshift. This fact is more evident at larger redshifts, where the centers of the voids are $\sim 40\%$ more underdense in galaxies than dark matter and the ridges of the voids are $\sim 15\%$ more overdense in galaxies than dark matter. We also find that, at all redshifts, there is a linear relationship between the galaxy and dark matter distributions that persists to radii $\sim 1.2R_{\text{eff}}$. The slope of this relationship varies over time in accordance with the estimates of the linear clustering bias that exists within the simulation.

The differences between the dark and luminous void density profiles decrease with decreasing redshift as dark matter leaves the centers of voids and populates the void ridges. The density of galaxies in the centers of voids remains relatively constant over time while the density of galaxies around void ridges fluctuate between ~ 0.16 at $z = 3.0$ to ~ 0.29 at $z = 0.2$ and ~ 0.18 at $z = 0.0$. That is, the centers of voids remain entirely devoid of galaxies, implying little to no net flow of galaxies into or out of TNG300 voids between $z = 3.0$ and $z = 0.0$. Our results for TNG300 voids thus demonstrate that, as traced by galaxies from $z = 3.0$ to $z = 0.0$, the radial density profiles of voids experience only slight trends in their evolution within fluctuations.

We also identified distinct “void-in-void” and “void-in-cloud” populations in each snapshot. From this, we find the interiors of all voids, regardless of hierarchy, are nearly devoid of galaxies, and they become more underdense in dark matter over time. Differences that exist between the integrated profiles of “voids-in-voids” and “voids-in-clouds” occur primarily at the void ridges. For instance, the number density contrast of galaxies remains constant over time within the ridges of “voids-in-clouds,” while the number density contrast of dark matter particles increases over time and becomes equal to that of the galaxies at $z = 0.0$. Between redshifts $z = 3.0$ and $z = 0.7$, the ridges of “voids-in-voids” tend to be more overdense in dark matter than in galaxies, while at lower redshifts, the ratios of galaxies to dark matter within the ridges of “voids-in-voids” approach unity.

The fluctuations in Δ_{\max} along void ridges could be indicative of a shift of the maximum density to slightly larger void radii at later times. We report such a shift in Figure 6b)-d), but it is more pronounced along the ridges of “voids-in-clouds” than it is for “voids-in-voids”. For instance, when both galaxies and dark matter are used as tracers of “voids-in-clouds,” Figure 6d) shows that R_{\max} increases from $1.42 \pm 0.08R_{\text{eff}}$ at $z = 0.2$ to $1.75 \pm 0.08R_{\text{eff}}$ at $z = 0.0$. Meanwhile, for “voids-in-voids,” $R_{\max, \text{DM}}$ fluctuates between $1.58 \pm 0.08R_{\text{eff}}$ at $z = 0.3$, $1.92 \pm 0.08R_{\text{eff}}$ at $z = 0.2$, $1.75 \pm 0.08R_{\text{eff}}$ at $z = 0.1$, and $1.92 \pm 0.08R_{\text{eff}}$ at $z = 0.0$ while $R_{\max, \text{galaxies}}$ increases from $1.58 \pm 0.08R_{\text{eff}}$ at $z = 0.3$ to $1.75 \pm 0.08R_{\text{eff}}$ at $z = 0.2$ and $1.92 \pm 0.08R_{\text{eff}}$ at $z = 0.0$. Investigating this result with a larger sample of resolved voids is beyond the scope of this manuscript, but it would help clarify whether or not this is a result of selection effects and small number statistics.

At early to intermediate redshifts, “voids-in-clouds” experience an influx of dark matter into their ridges. In contrast, “voids-in-voids” experience a loss of dark matter from their ridges. This implies that care should be taken when attempting to use galaxies as a tracer of dark matter in observations of voids at intermediate to high redshifts, since the actual density contrast of dark matter in the ridges of voids may be either higher or lower than the density contrast of the galaxies depending on the void environment.

Most studies of voids in cosmological simulations limit their analyses to redshifts $z \lesssim 0.7$ (see, e.g., [Paillas et al. 2017](#); [Habouzit et al. 2020](#); [Dávila-Kurbán et al. 2023](#); [Schuster et al. 2023](#)), so it is difficult to directly compare all our results to these studies. Despite the use of different voidfinder algorithms or trimming methods, however, our TNG300 ZOBOV voids are comparable to voids found in the EAGLE, HorizonAGN, and Magneticum simulations, and it is reasonable to discuss our results in the context of some of these investigations. First, while [Pollina et al. \(2017\)](#) focused on how b_{slope} varied as a function of void size in the $z = 0.14$ snapshot of the midres run of the Magneticum Pathfinder simulation, we studied the tracer-matter relationship from $z = 3.0$ to $z = 0.0$, finding a linear trend between δ_{gal} and δ_{DM} at all redshifts, and a slope that increases over time. [Pollina et al. \(2017\)](#) identified 36,430 voids in the galaxy field of the simulation, which covers a box that is $2,688h^{-1}\text{Mpc}$ on a side. Compared to the smallest voids that [Pollina et al. \(2017\)](#) examined (i.e., those with radii between $20 - 30h^{-1}\text{Mpc}$), we report smaller values of b_{slope} at $z = 0.1$ (1.26 ± 0.02 in our study vs. 2.164 ± 0.061 in [Pollina et al. 2017](#)). This is likely a direct result of the

sparser tracer population ($n_t \sim 5 \times 10^{-4} h^3 \text{Mpc}^{-3}$ in their study vs. $n_t \sim 3.9 \times 10^{-2} h^3 \text{Mpc}^{-3}$ in our study at $z = 0.1$), but it could also be caused by the different resolution elements for the dark matter ($4.0 \times 10^7 h^{-1} M_\odot$ for TNG300 and $1.3 \times 10^{10} h^{-1} M_\odot$ for Magneticum midres) and baryons ($7.5 \times 10^6 h^{-1} M_\odot$ for TNG300 and $2.6 \times 10^9 h^{-1} M_\odot$ for Magneticum midres), both of which can affect clustering bias (see, e.g., [Nadathur & Hotchkiss 2015](#); [Pollina et al. 2016](#)). However, our results agree with the general conclusions of [Pollina et al. \(2017\)](#) in that, within voids, there is a linear relationship between δ_{gal} and δ_{DM} , and the slope of this relationship is comparable to the clustering bias between the underlying matter distribution and a similarly selected tracer population.

[Habouzit et al. \(2020\)](#) identified 36 voids with a median radius of $3.8 h^{-1} \text{Mpc}$ and a median volume of $230 h^{-3} \text{Mpc}^3$ within the galaxy field of HorizonAGN. This simulation has dark matter and stellar mass resolution elements of $8 \times 10^7 M_\odot$ and $2 \times 10^6 M_\odot$, respectively. Although [Habouzit et al. \(2020\)](#) use a similar galaxy selection as we do (i.e., galaxies more massive than $2 \times 10^8 M_\odot$), the simulation has a comoving box length of $100 h^{-1} \text{Mpc}$, which is half the box length of TNG300 (i.e., one eighth of the volume, making identification of the largest structures in TNG300 not possible in HorizonAGN). [Habouzit et al. \(2020\)](#) also used a version of ZOBOV that adopted somewhat different conditions for merging underdense regions together to build the overall void hierarchy, and it is unclear how this will affect definitions of “voids-in-voids” and “voids-in-clouds”. Thus, although our TNG300 voids at $z = 0.0$ are larger and more abundant than those in HorizonAGN, this is likely attributable to the larger volume of TNG300 and differences in how underdense regions were merged together.

[Paillas et al. \(2017\)](#) used a 3DSVF to identify $\sim 10^3$ voids in the subhalo field of the EAGLE simulation at $z = 0.0$. This simulation has a comoving box size of 100Mpc^3 and has dark matter and baryon resolution elements of $9.7 \times 10^6 M_\odot$ and $1.81 \times 10^6 M_\odot$, respectively. These authors used a modified version of the 3DSVF that was developed by [Padilla et al. \(2005\)](#), where they modified the algorithm to test how the degree of allowable overlap between void regions affects their void catalogs. [Paillas et al. \(2017\)](#) created void catalogs for a variety of tracer populations. Among these, the tracer population most comparable to our study consists of all subhalos with stellar masses $\geq 10^8 M_\odot$, containing 40,076 total subhalos and resulting in a tracer number density of $n_t \sim 0.13 h^3 \text{Mpc}^{-3}$ ($n_t \sim 0.039 h^3 \text{Mpc}^{-3}$ at $z = 0.0$ in our study) and an average

void size of 7.1Mpc. The most significant difference between their radial density profiles and those that we obtained is that the centers of EAGLE voids reach a minimum galaxy density contrast of ~ -0.95 , a 5% increase over what we find for the centers of TNG300 voids. However, all other trends are consistent between the two simulations. For example, at $z = 0.0$, the ridges of EAGLE voids and TNG300 voids reach similar galaxy number density contrasts. Similarly, both populations have interior dark matter density contrasts of ~ -0.8 and ridges that peak at ~ 0.15 .

Schuster et al. (2023) used ZOBOV to study dark matter radial density profiles of voids identified in the halo and mass fields of the midres, highres, and ultra-hr runs of the Magneticum simulation. These runs have box lengths of $2, 688h^{-1}\text{Mpc}$, $640h^{-1}\text{Mpc}$, and $48h^{-1}\text{Mpc}$, dark matter particle counts of $2 \times 4, 536^3$, $2 \times 2, 880^3$, and 2×576^3 , and dark matter (baryon) resolution elements of $1.3 \times 10^{10}h^{-1}M_{\odot}$ ($2.6 \times 10^9h^{-1}M_{\odot}$), $6.9 \times 10^8h^{-1}M_{\odot}$ ($1.4 \times 10^8h^{-1}M_{\odot}$), and $3.6 \times 10^7h^{-1}M_{\odot}$ ($7.3 \times 10^6h^{-1}M_{\odot}$), respectively. When halos are used as tracers, Schuster et al. (2023) apply mass cuts of $1.0 \times 10^{12}h^{-1}M_{\odot}$, $1.0 \times 10^{11}h^{-1}M_{\odot}$, and $1.3 \times 10^9h^{-1}M_{\odot}$, giving tracer number densities of $3.2 \times 10^{-3}h^3\text{Mpc}^{-3}$, $3.1 \times 10^{-2}h^3\text{Mpc}^{-3}$, and $1.2h^3\text{Mpc}^{-3}$, respectively ($n_t \sim 4.0 \times 10^{-2}h^3\text{Mpc}^{-3}$ in our study at $z = 0.0$). Although their *merged* void sample was trimmed with an imposed maximum zone-linking density, the voids they analyzed are generally similar to the ones we identify. They found that the dark matter distribution within voids varied as a function of void size and shape. Compared to our dark matter profile at $z = 0.0$, their stacked profile is similar, despite resolution differences between TNG300 and Magneticum. Similarly, Dávila-Kurbán et al. (2023) used a 3DSVF to examine integrated “void-in-void” and “void-in-cloud” profiles of TNG300 voids. At $z = 0.0$, the interiors and ridges of our “void-in-void” and “void-in-cloud” profiles are nearly identical to theirs, reaching similar minima and maxima despite different choices for the implementation of the voidfinding algorithm.

Using observational data, Douglass et al. (2023) identified voids in the Sloan Digital Sky Survey (SDSS; York et al. 2000) DR7 (Abazajian et al. 2009) and investigated how the profiles of voids identified with 3DSVFs differed from those identified with ZOBOV. In particular, the 3DSVF VoidFinder (El-Ad & Piran 1997; Hoyle & Vogeley 2004) identified voids with flatter interior profiles and ridges that were only slightly denser than the surrounding environment. Despite using the other two commonly used methods for trimming

raw ZOBOV catalogs, their $z = 0.0$ ZOBOV density profiles closely resemble the $z = 0.0$ luminous density profiles that we present here.

Hamaus et al. (2020) used ZOBOV to study void-galaxy cross-correlation functions in the SDSS Baryon Oscillation Spectroscopic Survey (BOSS; Dawson et al. 2013), where they imposed a minimum void radius to trim their raw catalogs. Compared to the voids that we identified at redshift $z \sim 0.5$, the ridges of their monopole profiles are similar, but their interiors are slightly more overdense in galaxies ($\xi_0 \sim -0.90$). Nadathur et al. (2019) and Woodfinden et al. (2022) also obtained cross-correlation functions for SDSS BOSS and SDSS extended BOSS (eBOSS; Alam et al. 2021) Data Releases. Both studies identified voids with ZOBOV, trimming their catalogs by imposing a minimum void radius. They found voids out to $z = 0.7$ with similar interiors to those that we present but with ridges that only reach values of $\xi_0 \sim 0.05$.

Forthcoming surveys will map the galaxy distribution in the observed universe to unprecedented depths, encompassing enormous volumes of space and dramatically enhancing our understanding of the growth of structure over the past ~ 12 Gyr, including the evolution of voids over cosmic time. Our results for TNG300 voids demonstrate that, as traced by galaxies, the radial density profiles of voids fluctuates from $z = 3.0$ to $z = 0.0$, and the relationship between void galaxy density contrast and dark matter density contrast is consistent with linear bias over this time period. If Λ CDM is the correct model of structure formation, then, future void surveys should yield similar conclusions for voids in the observed universe.

While using galaxies to obtain radial density profiles for voids as a function of redshift should be relatively straightforward (given sufficiently deep observations), testing the evolution of the void galaxy-dark matter bias relationship that we obtained will depend on the ability to directly constrain the mass density profiles of voids over a similar redshift range. This may be possible in future because, although highly challenging to carry out, (see, e.g., Izumi et al. 2013; Barreira et al. 2015; Sánchez et al. 2017; Paillas et al. 2019; Bonici et al. 2023), precise weak lensing studies of voids hold the promise to constrain the relationship between void galaxies and dark matter in much the same way that weak lensing studies have constrained the galaxy-matter cross-correlation function for galaxies (see More et al. 2023 and references therein).

ACKNOWLEDGEMENTS

We are grateful to the anonymous reviewer for helpful comments and suggestions that improved the manuscript. This work was partially supported by the National Science Foundation grant AST-2009397. The TNG simulations were undertaken with compute time awarded by the Gauss Centre for Supercomputing (GCS) under GCS Large-Scale Projects GCS-ILLU and GCS-DWAR on the GCS share of the supercomputer Hazel Hen at the High Performance Computing Center Stuttgart (HLRS), as well as on the machines of the Max Planck Computing and Data Facility (MPCDF) in Garching, Germany. In addition, we are pleased to acknowledge that the computational work reported on in this paper was performed on the Shared Computing Cluster, administered by Boston University's Research Computing Services, and located at the Massachusetts Green High Performance Computing Center in Holyoke, MA. OC acknowledges support from the Penn State Extraterrestrial Intelligence Center. BM acknowledges support from Northeastern University's Future Faculty Postdoctoral Fellowship program.

REFERENCES

- Abazajian, K. N., Adelman-McCarthy, J. K., Agüeros, M. A., et al. 2009, *ApJS*, 182, 543, doi: [10.1088/0067-0049/182/2/543](https://doi.org/10.1088/0067-0049/182/2/543)
- Adermann, E., Elahi, P. J., Lewis, G. F., & Power, C. 2017, *MNRAS*, 468, 3381, doi: [10.1093/mnras/stx657](https://doi.org/10.1093/mnras/stx657)
- Alam, S., Aubert, M., Avila, S., et al. 2021, *PhRvD*, 103, 083533, doi: [10.1103/PhysRevD.103.083533](https://doi.org/10.1103/PhysRevD.103.083533)
- Aragon-Calvo, M. A., & Szalay, A. S. 2013, *MNRAS*, 428, 3409, doi: [10.1093/mnras/sts281](https://doi.org/10.1093/mnras/sts281)
- Barreira, A., Cautun, M., Li, B., Baugh, C. M., & Pascoli, S. 2015, *JCAP*, 2015, 028, doi: [10.1088/1475-7516/2015/08/028](https://doi.org/10.1088/1475-7516/2015/08/028)
- Behroozi, P. S., Loeb, A., & Wechsler, R. H. 2013, *JCAP*, 2013, 019, doi: [10.1088/1475-7516/2013/06/019](https://doi.org/10.1088/1475-7516/2013/06/019)
- Bonici, M., Carbone, C., Davini, S., et al. 2023, *A&A*, 670, A47, doi: [10.1051/0004-6361/202244445](https://doi.org/10.1051/0004-6361/202244445)
- Bothun, G. D., Geller, M. J., Kurtz, M. J., Huchra, J. P., & Schild, R. E. 1992, *ApJ*, 395, 347
- Cai, Y.-C., Neyrinck, M., Mao, Q., et al. 2017, *MNRAS*, 466, 3364, doi: [10.1093/mnras/stw3299](https://doi.org/10.1093/mnras/stw3299)
- Cautun, M., van de Weygaert, R., Jones, B. J. T., & Frenk, C. S. 2014, *MNRAS*, 441, 2923, doi: [10.1093/mnras/stu768](https://doi.org/10.1093/mnras/stu768)
- Ceccarelli, L., Padilla, N. D., Valotto, C., & Lambas, D. G. 2006, *MNRAS*, 373, 1440, doi: [10.1111/j.1365-2966.2006.11129.x](https://doi.org/10.1111/j.1365-2966.2006.11129.x)
- Ceccarelli, L., Paz, D., Lares, M., Padilla, N., & Lambas, D. G. 2013, *MNRAS*, 434, 1435, doi: [10.1093/mnras/stt1097](https://doi.org/10.1093/mnras/stt1097)

- Clampitt, J., Cai, Y.-C., & Li, B. 2013, *MNRAS*, 431, 749, doi: [10.1093/mnras/stt219](https://doi.org/10.1093/mnras/stt219)
- Colberg, J. M., Sheth, R. K., Diaferio, A., Gao, L., & Yoshida, N. 2005, *MNRAS*, 360, 216, doi: [10.1111/j.1365-2966.2005.09064.x](https://doi.org/10.1111/j.1365-2966.2005.09064.x)
- Contarini, S., Marulli, F., Moscardini, L., et al. 2021, *MNRAS*, 504, 5021, doi: [10.1093/mnras/stab1112](https://doi.org/10.1093/mnras/stab1112)
- Correa, C. M., Paz, D. J., Sánchez, A. G., et al. 2021, *MNRAS*, 500, 911, doi: [10.1093/mnras/staa3252](https://doi.org/10.1093/mnras/staa3252)
- Courtois, H. M., van de Weygaert, R., Aubert, M., et al. 2023, *A&A*, 673, A38, doi: [10.1051/0004-6361/202245578](https://doi.org/10.1051/0004-6361/202245578)
- Curtis, O., McDonough, B., & Brainerd, T. G. 2024, *ApJ*, 962, 58, doi: [10.3847/1538-4357/ad18b4](https://doi.org/10.3847/1538-4357/ad18b4)
- Dávila-Kurbán, F., Lares, M., & Lambas, D. G. 2023, *MNRAS*, 518, 3095, doi: [10.1093/mnras/stac3311](https://doi.org/10.1093/mnras/stac3311)
- Dawson, K. S., Schlegel, D. J., Ahn, C. P., et al. 2013, *AJ*, 145, 10, doi: [10.1088/0004-6256/145/1/10](https://doi.org/10.1088/0004-6256/145/1/10)
- Dolag, K., Komatsu, E., & Sunyaev, R. 2016, *MNRAS*, 463, 1797, doi: [10.1093/mnras/stw2035](https://doi.org/10.1093/mnras/stw2035)
- Domínguez-Gómez, J., Pérez, I., Ruiz-Lara, T., et al. 2023a, *Nature*, 619, 269, doi: [10.1038/s41586-023-06109-1](https://doi.org/10.1038/s41586-023-06109-1)
- . 2023b, *A&A*, 680, A111, doi: [10.1051/0004-6361/202346884](https://doi.org/10.1051/0004-6361/202346884)
- Douglass, K. A., Veyrat, D., & BenZvi, S. 2023, *ApJS*, 265, 7, doi: [10.3847/1538-4365/acabcf](https://doi.org/10.3847/1538-4365/acabcf)
- El-Ad, H., & Piran, T. 1997, *ApJ*, 491, 421, doi: [10.1086/304973](https://doi.org/10.1086/304973)
- Gregory, S. A., & Thompson, L. A. 1978, *ApJ*, 222, 784, doi: [10.1086/156198](https://doi.org/10.1086/156198)
- Habouzit, M., Pisani, A., Goulding, A., et al. 2020, *MNRAS*, 493, 899, doi: [10.1093/mnras/staa219](https://doi.org/10.1093/mnras/staa219)
- Hamaus, N., Pisani, A., Choi, J.-A., et al. 2020, *JCAP*, 2020, 023, doi: [10.1088/1475-7516/2020/12/023](https://doi.org/10.1088/1475-7516/2020/12/023)
- Hamaus, N., Sutter, P. M., Lavaux, G., & Wandelt, B. D. 2015, *JCAP*, 2015, 036, doi: [10.1088/1475-7516/2015/11/036](https://doi.org/10.1088/1475-7516/2015/11/036)
- Hamaus, N., Sutter, P. M., & Wandelt, B. D. 2014, *PhRvL*, 112, 251302, doi: [10.1103/PhysRevLett.112.251302](https://doi.org/10.1103/PhysRevLett.112.251302)
- Hamaus, N., Aubert, M., Pisani, A., et al. 2022, *A&A*, 658, A20, doi: [10.1051/0004-6361/202142073](https://doi.org/10.1051/0004-6361/202142073)
- Hirschmann, M., Dolag, K., Saro, A., et al. 2014, *MNRAS*, 442, 2304, doi: [10.1093/mnras/stu1023](https://doi.org/10.1093/mnras/stu1023)
- Hoyle, F., & Vogeley, M. S. 2004, *ApJ*, 607, 751, doi: [10.1086/386279](https://doi.org/10.1086/386279)
- Izumi, K., Hagiwara, C., Nakajima, K., Kitamura, T., & Asada, H. 2013, *PhRvD*, 88, 024049, doi: [10.1103/PhysRevD.88.024049](https://doi.org/10.1103/PhysRevD.88.024049)
- Kaiser, N. 1984, *ApJL*, 284, L9, doi: [10.1086/184341](https://doi.org/10.1086/184341)
- Kovač, K., Lilly, S. J., Knobel, C., et al. 2014, *MNRAS*, 438, 717, doi: [10.1093/mnras/stt2241](https://doi.org/10.1093/mnras/stt2241)
- Kreisch, C. D., Pisani, A., Villaescusa-Navarro, F., et al. 2022, *ApJ*, 935, 100, doi: [10.3847/1538-4357/ac7d4b](https://doi.org/10.3847/1538-4357/ac7d4b)
- Lavaux, G., & Wandelt, B. D. 2010, *MNRAS*, 403, 1392, doi: [10.1111/j.1365-2966.2010.16197.x](https://doi.org/10.1111/j.1365-2966.2010.16197.x)
- Lee, J., & Park, D. 2009, *ApJL*, 696, L10, doi: [10.1088/0004-637X/696/1/L10](https://doi.org/10.1088/0004-637X/696/1/L10)
- Li, B., Zhao, G.-B., & Koyama, K. 2012, *MNRAS*, 421, 3481, doi: [10.1111/j.1365-2966.2012.20573.x](https://doi.org/10.1111/j.1365-2966.2012.20573.x)

- Mao, Q., Berlind, A. A., Scherrer, R. J., et al. 2017, *ApJ*, 835, 161, doi: [10.3847/1538-4357/835/2/161](https://doi.org/10.3847/1538-4357/835/2/161)
- Marinacci, F., Vogelsberger, M., Pakmor, R., et al. 2018, *MNRAS*, 480, 5113, doi: [10.1093/mnras/sty2206](https://doi.org/10.1093/mnras/sty2206)
- Mo, H. J., & White, S. D. M. 1996, *MNRAS*, 282, 347, doi: [10.1093/mnras/282.2.347](https://doi.org/10.1093/mnras/282.2.347)
- More, S., Sugiyama, S., Miyatake, H., et al. 2023, *PhRvD*, 108, 123520, doi: [10.1103/PhysRevD.108.123520](https://doi.org/10.1103/PhysRevD.108.123520)
- Nadathur, S. 2016, *MNRAS*, 461, 358, doi: [10.1093/mnras/stw1340](https://doi.org/10.1093/mnras/stw1340)
- Nadathur, S., Carter, P. M., Percival, W. J., Winther, H. A., & Bautista, J. E. 2019, *PhRvD*, 100, 023504, doi: [10.1103/PhysRevD.100.023504](https://doi.org/10.1103/PhysRevD.100.023504)
- Nadathur, S., & Hotchkiss, S. 2014, *MNRAS*, 440, 1248, doi: [10.1093/mnras/stu349](https://doi.org/10.1093/mnras/stu349)
- . 2015, *MNRAS*, 454, 889, doi: [10.1093/mnras/stv1994](https://doi.org/10.1093/mnras/stv1994)
- Nadathur, S., Hotchkiss, S., Diego, J. M., et al. 2015, *MNRAS*, 449, 3997, doi: [10.1093/mnras/stv513](https://doi.org/10.1093/mnras/stv513)
- Nadathur, S., Lavinto, M., Hotchkiss, S., & Räsänen, S. 2014, *PhRvD*, 90, 103510, doi: [10.1103/PhysRevD.90.103510](https://doi.org/10.1103/PhysRevD.90.103510)
- Naiman, J. P., Pillepich, A., Springel, V., et al. 2018, *MNRAS*, 477, 1206, doi: [10.1093/mnras/sty618](https://doi.org/10.1093/mnras/sty618)
- Nelson, D., Pillepich, A., Springel, V., et al. 2018, *MNRAS*, 475, 624, doi: [10.1093/mnras/stx3040](https://doi.org/10.1093/mnras/stx3040)
- Neyrinck, M. C. 2008, *MNRAS*, 386, 2101, doi: [10.1111/j.1365-2966.2008.13180.x](https://doi.org/10.1111/j.1365-2966.2008.13180.x)
- Owusu, S., da Silveira Ferreira, P., Notari, A., & Quartin, M. 2023, *JCAP*, 2023, 040, doi: [10.1088/1475-7516/2023/06/040](https://doi.org/10.1088/1475-7516/2023/06/040)
- Padilla, N. D., Ceccarelli, L., & Lambas, D. G. 2005, *MNRAS*, 363, 977
- Paillas, E., Cautun, M., Li, B., et al. 2019, *MNRAS*, 484, 1149, doi: [10.1093/mnras/stz022](https://doi.org/10.1093/mnras/stz022)
- Paillas, E., Lagos, C. D. P., Padilla, N., et al. 2017, *MNRAS*, 470, 4434, doi: [10.1093/mnras/stx1514](https://doi.org/10.1093/mnras/stx1514)
- Panchal, R. R., Pisani, A., & Spergel, D. N. 2020, *ApJ*, 901, 87, doi: [10.3847/1538-4357/abaddf](https://doi.org/10.3847/1538-4357/abaddf)
- Park, D., & Lee, J. 2007, *PhRvL*, 98, 081301, doi: [10.1103/PhysRevLett.98.081301](https://doi.org/10.1103/PhysRevLett.98.081301)
- Patiri, S. G., Betancort-Rijo, J., & Prada, F. 2012, *A&A*, 541, L4, doi: [10.1051/0004-6361/201219036](https://doi.org/10.1051/0004-6361/201219036)
- Paz, D., Lares, M., Ceccarelli, L., Padilla, N., & Lambas, D. G. 2013, *MNRAS*, 436, 3480, doi: [10.1093/mnras/stt1836](https://doi.org/10.1093/mnras/stt1836)
- Paz, D. J., Correa, C. M., Gualpa, S. R., et al. 2023, *MNRAS*, 522, 2553, doi: [10.1093/mnras/stad1146](https://doi.org/10.1093/mnras/stad1146)
- Peebles, P. J. E. 1980, *The large-scale structure of the universe* (Princeton university press)
- . 1993, *Principles of Physical Cosmology* (Princeton university press), doi: [10.1515/9780691206721](https://doi.org/10.1515/9780691206721)
- Pellicciari, D., Contarini, S., Marulli, F., et al. 2023, *MNRAS*, 522, 152, doi: [10.1093/mnras/stad956](https://doi.org/10.1093/mnras/stad956)
- Pillepich, A., Nelson, D., Hernquist, L., et al. 2018, *MNRAS*, 475, 648, doi: [10.1093/mnras/stx3112](https://doi.org/10.1093/mnras/stx3112)
- Planck Collaboration, Ade, P. A. R., Aghanim, N., et al. 2016, *A&A*, 594, A13, doi: [10.1051/0004-6361/201525830](https://doi.org/10.1051/0004-6361/201525830)

- Platen, E., van de Weygaert, R., & Jones, B. J. T. 2007, MNRAS, 380, 551, doi: [10.1111/j.1365-2966.2007.12125.x](https://doi.org/10.1111/j.1365-2966.2007.12125.x)
- Pollina, G., Baldi, M., Marulli, F., & Moscardini, L. 2016, MNRAS, 455, 3075, doi: [10.1093/mnras/stv2503](https://doi.org/10.1093/mnras/stv2503)
- Pollina, G., Hamaus, N., Dolag, K., et al. 2017, MNRAS, 469, 787, doi: [10.1093/mnras/stx785](https://doi.org/10.1093/mnras/stx785)
- Pollina, G., Hamaus, N., Paech, K., et al. 2019, MNRAS, 487, 2836, doi: [10.1093/mnras/stz1470](https://doi.org/10.1093/mnras/stz1470)
- Ricciardelli, E., Quilis, V., & Varela, J. 2014, MNRAS, 440, 601, doi: [10.1093/mnras/stu307](https://doi.org/10.1093/mnras/stu307)
- Rodríguez Medrano, A. M., Paz, D. J., Stasyszyn, F. A., & Ruiz, A. N. 2022, MNRAS, 511, 2688, doi: [10.1093/mnras/stac127](https://doi.org/10.1093/mnras/stac127)
- Rodríguez-Medrano, A. M., Springel, V., Stasyszyn, F. A., & Paz, D. J. 2024, MNRAS, doi: [10.1093/mnras/stae193](https://doi.org/10.1093/mnras/stae193)
- Sánchez, C., Clampitt, J., Kovacs, A., et al. 2017, MNRAS, 465, 746, doi: [10.1093/mnras/stw2745](https://doi.org/10.1093/mnras/stw2745)
- Schaap, W. E. 2007, PhD thesis, University of Groningen, Netherlands
- Schuster, N., Hamaus, N., Dolag, K., & Weller, J. 2023, JCAP, 2023, 031, doi: [10.1088/1475-7516/2023/05/031](https://doi.org/10.1088/1475-7516/2023/05/031)
- Schuster, N., Hamaus, N., Pisani, A., et al. 2019, JCAP, 2019, 055, doi: [10.1088/1475-7516/2019/12/055](https://doi.org/10.1088/1475-7516/2019/12/055)
- Shandarin, S. F., & Zeldovich, Y. B. 1989, Reviews of Modern Physics, 61, 185, doi: [10.1103/RevModPhys.61.185](https://doi.org/10.1103/RevModPhys.61.185)
- Sheth, R. K., & van de Weygaert, R. 2004, MNRAS, 350, 517, doi: [10.1111/j.1365-2966.2004.07661.x](https://doi.org/10.1111/j.1365-2966.2004.07661.x)
- Springel, V., White, S. D. M., Tormen, G., & Kauffmann, G. 2001, MNRAS, 328, 726, doi: [10.1046/j.1365-8711.2001.04912.x](https://doi.org/10.1046/j.1365-8711.2001.04912.x)
- Springel, V., White, S. D. M., Jenkins, A., et al. 2005, Nature, 435, 629
- Springel, V., Pakmor, R., Pillepich, A., et al. 2018, MNRAS, 475, 676, doi: [10.1093/mnras/stx3304](https://doi.org/10.1093/mnras/stx3304)
- Sutter, P. M., Elahi, P., Falck, B., et al. 2014a, MNRAS, 445, 1235, doi: [10.1093/mnras/stu1845](https://doi.org/10.1093/mnras/stu1845)
- Sutter, P. M., Lavaux, G., Hamaus, N., et al. 2014b, MNRAS, 442, 462, doi: [10.1093/mnras/stu893](https://doi.org/10.1093/mnras/stu893)
- Sutter, P. M., Lavaux, G., Wandelt, B. D., & Weinberg, D. H. 2012, ApJ, 761, 44, doi: [10.1088/0004-637X/761/1/44](https://doi.org/10.1088/0004-637X/761/1/44)
- Sutter, P. M., Lavaux, G., Hamaus, N., et al. 2015, Astronomy and Computing, 9, 1, doi: [10.1016/j.ascom.2014.10.002](https://doi.org/10.1016/j.ascom.2014.10.002)
- Tifft, W. G., & Gregory, S. A. 1976, ApJ, 205, 696, doi: [10.1086/154325](https://doi.org/10.1086/154325)
- Tinker, J. L., Robertson, B. E., Kravtsov, A. V., et al. 2010, ApJ, 724, 878, doi: [10.1088/0004-637X/724/2/878](https://doi.org/10.1088/0004-637X/724/2/878)
- Tully, R. B., Courtois, H. M., & Sorce, J. G. 2016, AJ, 152, 50, doi: [10.3847/0004-6256/152/2/50](https://doi.org/10.3847/0004-6256/152/2/50)
- Tully, R. B., & Fisher, J. R. 1987, Nearby galaxies Atlas (Cambridge University Press)
- Tully, R. B., Pomarède, D., Graziani, R., et al. 2019, ApJ, 880, 24, doi: [10.3847/1538-4357/ab2597](https://doi.org/10.3847/1538-4357/ab2597)
- Vallés-Pérez, D., Quilis, V., & Planelles, S. 2021, ApJL, 920, L2, doi: [10.3847/2041-8213/ac2816](https://doi.org/10.3847/2041-8213/ac2816)
- van de Weygaert, R., & van Kampen, E. 1993, MNRAS, 263, 481

- van Haarlem, M., & van de Weygaert, R. 1993, *ApJ*, 418, 544, doi: [10.1086/173416](https://doi.org/10.1086/173416)
- Villaescusa-Navarro, F., Vogelsberger, M., Viel, M., & Loeb, A. 2013, *MNRAS*, 431, 3670, doi: [10.1093/mnras/stt452](https://doi.org/10.1093/mnras/stt452)
- Wang, B. Y., & Pisani, A. 2024, *ApJL*, 970, L32, doi: [10.3847/2041-8213/ad5ffe](https://doi.org/10.3847/2041-8213/ad5ffe)
- Wojtak, R., Powell, D., & Abel, T. 2016, *MNRAS*, 458, 4431, doi: [10.1093/mnras/stw615](https://doi.org/10.1093/mnras/stw615)
- Woodfinden, A., Nadathur, S., Percival, W. J., et al. 2022, *MNRAS*, 516, 4307, doi: [10.1093/mnras/stac2475](https://doi.org/10.1093/mnras/stac2475)
- York, D. G., Adelman, J., Anderson, John E., J., et al. 2000, *AJ*, 120, 1579, doi: [10.1086/301513](https://doi.org/10.1086/301513)
- Zel'dovich, Y. B. 1970, *A&A*, 5, 84
- Zhang, C., Churazov, E., Dolag, K., Forman, W. R., & Zhuravleva, I. 2020, *MNRAS*, 494, 4539, doi: [10.1093/mnras/staa1013](https://doi.org/10.1093/mnras/staa1013)
- Zivick, P., Sutter, P. M., Wandelt, B. D., Li, B., & Lam, T. Y. 2015, *MNRAS*, 451, 4215, doi: [10.1093/mnras/stv1209](https://doi.org/10.1093/mnras/stv1209)